NASA
Technical
Paper
3285

April 1993

Description of Alpha-Nucleus Interaction Cross Sections for Cosmic Ray Shielding Studies

Francis A. Cucinotta,
Lawrence W. Townsend,
and John W. Wilson

NASA Technical Paper 3285

1993

Description of Alpha-Nucleus Interaction Cross Sections for Cosmic Ray Shielding Studies

Francis A. Cucinotta,
Lawrence W. Townsend,
and John W. Wilson
Langley Research Center
Hampton, Virginia

National Aeronautics and Space Administration
Office of Management
Scientific and Technical Information Program

Abstract

Nuclear interactions of high-energy alpha particles with target nuclei important for cosmic ray studies are discussed. Models for elastic, quasi-elastic, and breakup reactions are presented and compared with experimental data. Energy-dependent interaction cross sections and secondary spectra are presented based on theoretical models and the limited experimental data base.

1. Introduction

In this paper we consider theoretical models of alpha-nucleus interactions for the purpose of developing a data base for describing the transport of cosmic ray alpha particles (^{4}He) and secondary light ions through bulk materials. Alpha (α) particles represent about 10–12 percent of the primary galactic cosmic ray flux, second only to the hydrogen component, which represents 86–89 percent of the abundance. Interaction cross sections for ^{4}He–^{1}H collisions have long been of interest (refs. 1–3) in the understanding of the chemical composition of the primary cosmic radiation because their interaction is the chief mechanism for ^{2}H and ^{3}He productions which are absent from the primary sources. More recently, the possibility of long-duration manned missions beyond the Earth's orbit has resulted in an increased effort to understand the possible late and genetic effects of galactic cosmic radiation (ref. 4) and to accurately predict the exposures to be encountered. The large primary alpha component and also the important secondary alpha component from the fragmentation of heavier elements warrant a study of their physical interactions in spacecraft materials and tissue.

The internal structure of ^{4}He, which is unique in several aspects, suggests an individual treatment of the physical interactions. First, this nucleus is the most compact with charge (matter) radius of 1.67 fm (1.33 fm) in comparison with the lighter nuclei ^{2}H and ^{3}He with charge (matter) radius of 2.1 fm (1.71 fm) and 1.88 fm (1.45 fm), respectively. The compactness of ^{4}He is an indication of the large binding energy at about 7 MeV/particle and results in a first excited state far removed from the ground state at about 20 MeV. Similar to the other light ions with mass number $A < 5$, no bound excited states occur for ^{4}He. We note that the first excitation level of all other nuclei occurs at only a few MeV. Nuclear correlations of dynamical content are expected to be enhanced because of this compactness which is, in part, due to the absence of Pauli exclusion effects and to the closed shell structure. The $A = 2, 3$ nuclei are now amenable to exact solution for their internal wave functions using realistic nucleon-nucleon interactions (refs. 5–8). This is not true for ^{4}He, although variational Monte Carlo approaches have been used (refs. 9–12). Also, nuclear matter or independent particle models used for the study of heavy ions are expected to fail for ^{4}He where the concept of a mean field does not hold. Finally, the description of nuclear fragmentation for light nuclei will be in terms of a one-step process of direct reaction, rather than the abrasion-ablation picture used for describing heavy-ion fragmentation (ref. 13).

The interaction cross sections for alpha projectiles consist of the elastic channel, compound nucleus reactions, stripping and pickup channels, and the fragmentation reactions. For cosmic ray studies these cross sections are needed over the energy range from a few MeV to above $100A$ GeV. However, because of the dominance of atomic/molecular interactions at low energies (including the resulting short range of the ions) and the small primary flux above about $10A$ GeV, the energy range from above a few 10's of A MeV to about $10A$ GeV is most important. The nuclear absorption cross section imposes an important constraint on the sum of the inelastic channel cross sections. A second-order solution (refs. 14 and 15) to the coupled channel equations (refs. 16 and 17) of the optical model in the eikonal approximation has been developed. The absorption cross sections and elastic scattering distributions for alpha-nucleus collisions are

calculated by using a realistic model for the ^{4}He ground-state one- and two-body densities. The total scattering cross section is also evaluated.

An important effect that results from the large separation energy for the first excited state in ^{4}He is a significant cross section for inelastic reactions with composite nuclei where the alpha particle remains intact; i.e., the target nucleus fragments while the projectile alpha particle does not fragment. This quasi-elastic type of reaction has been described by the optical model (refs. 18 and 19) and is applied here to estimate the fractional contribution of quasi-elastic processes to the absorption cross section for common shielding materials.

The fragmentation of light nuclei is often described by a single pole diagram (refs. 20–22) in which a single nucleon or cluster reacts on the target with the remaining piece of the ion acting only as a spectator. This type of impulse approximation fails when an extended region of the kinematical phase space is considered. We have developed an effective three-body multiple scattering approach (refs. 23 and 24) to describe the two-body dissociation of light nuclei on composite targets. The effects of elastic and inelastic fragmentation and final-state interactions are treated in this model. For ^{4}He this model describes the ^{3}H-p, ^{3}He-n, and d-d final states. Interactions of knocked-out clusters with the target are described by the optical model of multiple scattering, and thus the energy dependence of these ^{4}He fragmentation channels is described. We apply this model to calculate integrated cross sections and compare the calculations with available experimental data. Deuteron production cross sections from ^{3}He and ^{3}H projectiles and the breakup of ^{2}H may also be evaluated in this model.

The two-body dissociation states and the quasi-elastic scattering account for roughly half of the absorption cross section when meson production is included. At low energies the stripping reactions are important, but their importance decreases at high energies because the amplitude involves the dissociation vertex in an energy-dependent manner. Extensive measurements have been made for pickup on ^{1}H for ^{4}He projectiles. We use the Serber model (refs. 25 and 26) to obtain a mass number dependent scaling of these experiments. Estimates of compound nucleus cross sections can be provided from the EVAP-4 code of reference 27 for light-ion projectiles below $100A$ MeV. The remainder of the absorption cross section is shared by the $\alpha \rightarrow dpn$ and $\alpha \rightarrow npnp$ channels. Theoretical models of these reactions are hampered by the complexity of the many body final states and the fact that the vertex functions for these breakup modes have not been evaluated in any realistic model. We note that semiphenomenological methods have been used with some success for the $\alpha \rightarrow dpn$ breakup (ref. 28).

The outline of this paper is as follows: First, the optical model is used to evaluate total, absorption, and elastic scattering cross sections that are compared with experimental data. The calculation of the quasi-elastic cross section for inelastically scattered alpha particles is then described, and predictions for common shielding materials are made. Second, the model of two-body dissociation of light ions is used to predict energy-dependent fragmentation cross sections. The Serber model for pickup and stripping is used to estimate these cross sections for alpha projectiles. Third, and finally, a survey of the available experimental data is made and combined with theoretical predictions to give energy-dependent parameterizations of cross sections for secondary ^{4}He, ^{3}He, ^{3}H, ^{2}H, and ^{1}H in alpha-nucleus collisions. A parameterization for the energy spectrum of secondaries is also presented.

2. The Elastic Channel and Nuclear Absorption

The evaluation of the nuclear absorption cross section proceeds from the elastic scattering amplitude and the optical theorem. In the Eikonal coupled channels (ECC) model (refs. 14 and 16), the matrix of scattering amplitudes for all possible projectile-target transitions is given by

$$\overline{f}(\mathbf{q}) = \frac{ik}{2\pi}\widehat{Z}\int d^2b\; e^{i\mathbf{q}\cdot\mathbf{b}}\left\{e^{i\bar{\chi}(\mathbf{b})} - \bar{1}\right\} \tag{1}$$

where barred quantities represent matrices and bold quantities represent vectors. Here, $\mathbf{b}$ is the impact parameter vector, $\mathbf{q}$ is the momentum transfer vector, and k is the projectile-target relative wave number. In equation (1), $\widehat{Z}$ is an ordering operator for the z-coordinate which is necessary only when noncommuting two-body interactions are considered. The phase elements of $\overline{\chi}$ are defined by matrix elements of arbitrary projectile-target states of the operator

$$\widehat{\chi}(\mathbf{b}) = \sum_{\alpha,j} \frac{-\mu}{2k} \int_{-\infty}^{\infty} dz \; t_{\alpha j}(\mathbf{r}_\alpha - \mathbf{r}_j + \mathbf{x}) \tag{2}$$

where μ is the nucleus-nucleus reduced mass, α and j label the projectile and target constituents, respectively, $\mathbf{r}$ is the internal coordinate, $\mathbf{x}$ is the relative coordinate with $\mathbf{x} = (\mathbf{b}, z)$, and $t_{\alpha j}$ is the free two-body scattering amplitude in the overall center-of-mass frame. For a projectile transition from quantum state n to n' and target transition from ν to ν', we write

$$\chi_{n\nu,n'\nu'}(\mathbf{b}) = \sum_{\alpha,j}^{A_P,A_T} \frac{-\mu}{2k} \int_{-\infty}^{+\infty} dz' < n\nu|t_{\alpha j}|n'\nu' > \tag{3}$$

where A_P and A_T denote the mass numbers of projectile and target, respectively. Equation (3) is written in terms of transition densities ρ as

$$\chi_{n\nu,n'\nu'}(\mathbf{b}) = \frac{-\mu}{2k} \sum_{\alpha j} \int_{-\infty}^{\infty} dz \int d\mathbf{r}_\alpha \; d\mathbf{r}_j \; \rho_{\nu\nu'}(\mathbf{r}_j) \; \rho_{nn'}(\mathbf{r}_\alpha) \; t_{\alpha j}(\mathbf{r}_\alpha + \mathbf{r}_j - \mathbf{x}) \tag{4}$$

or in terms of transition form factors as

$$\chi_{n\nu,n'\nu'}(\mathbf{b}) = \frac{-\mu}{2k(2\pi)^3} \sum_{\alpha j} \int_{-\infty}^{\infty} dz \int d\mathbf{q} \; e^{i\mathbf{q}\cdot x} \; F_{nn'}(-\mathbf{q}) \; G_{\nu\nu'}(\mathbf{q}) \; t_{\alpha j}(\mathbf{q}) \tag{5}$$

where F and G are the projectile and target one-body form factors, respectively.

The two-body amplitudes must be related to their values in the nucleon-nucleon (NN) center-of-mass (CM) frame where the physical amplitude f_{NN} is determined by experiments. Making this transformation and noting that the z-integration in equation (5) can be performed formally if commuting interactions are assumed reduces equation (5) to

$$\chi_{n\nu,n'\nu'}(\mathbf{b}) = \frac{1}{2\pi k_{\mathrm{NN}}} \sum_{\alpha j} \int d^2q \; e^{i\mathbf{q}\cdot\mathbf{b}} \; F_{nn'}(-\mathbf{q}) \; G_{\nu\nu'}(\mathbf{q}) \; f_{\mathrm{NN}}(q) \tag{6}$$

where f_{NN} is the two-body scattering amplitude in the NN CM frame. Equation (6) is convenient for calculations since it is essentially a one-dimensional integration if the form factors are known.

The second-order approximation to the elastic (EL) amplitude is obtained by including all transitions between the ground and excited states and assuming that transitions between excited states are negligible. Furthermore, the density of all excited (EXC) states is approximated by an average excited-state density. The phase matrix is then of the bordered form

$$\overline{\chi}(\mathbf{b}) = \begin{pmatrix} \chi_{\mathrm{EL}} & \chi_{00,01} & \chi_{00,10} & \chi_{00,11} & \cdots \\ \chi_{01,00} & \chi_{\mathrm{EXC}} & 0 & 0 & \cdots \\ \chi_{10,00} & 0 & \chi_{\mathrm{EXC}} & 0 & \cdots \\ \chi_{11,00} & 0 & 0 & \chi_{\mathrm{EXC}} & \cdots \\ \vdots & \vdots & \vdots & \vdots & \end{pmatrix} \tag{7}$$

where $\chi_{EL} = \chi_{00,00}$. The characteristic equation of this bordered matrix is

$$(\chi_{EXC} - \lambda)^{N_0-2}\left[(\chi_{EL} - \lambda)(\chi_{EXC} - \lambda) - \Upsilon^2\right] = 0 \tag{8}$$

where N_0 is the order of $\overline{\chi}$, λ is the eigenvalue, and Υ^2 is defined by

$$\Upsilon^2(\mathbf{b}) = \sum_{n \text{ or } \nu \neq 0} \chi_{00,n\nu}\chi_{n\nu,00} \tag{9}$$

The eigenvalues are then given by

$$\lambda_{1,2} = \frac{1}{2}(\chi_{EL} + \chi_{EXC}) \pm \left\{\left[\frac{1}{2}(\chi_{EL} - \chi_{EXC})\right]^2 + \Upsilon^2\right\}^{1/2} \tag{10}$$

with all others taking the value χ_{EXC}. The form of the eigenvalues allows us to treat the scattering system as an effective two-channel problem with

$$\overline{\chi} = \begin{pmatrix} \chi_{EL} & \Upsilon \\ \Upsilon & \chi_{EXC} \end{pmatrix} \tag{11}$$

Then, from employing Sylvester's theorem we find that

$$f_{CC}^{(2)}(\mathbf{q}) = \frac{-ik}{2\pi}\int e^{-i\mathbf{q}\cdot\mathbf{b}}\left\{\exp\left[\frac{1}{2}i(\chi_{EL} + \chi_{EXC})\right]\right.$$

$$\left.\times\left[\cos\left(\chi_{DIF}^2 + \Upsilon^2\right)^{1/2} + i\chi_{DIF}\frac{\sin\left(\chi_{DIF}^2 + \Upsilon^2\right)^{1/2}}{\left(\chi_{DIF}^2 + \Upsilon^2\right)^{1/2}}\right] - 1\right\} d^2b \tag{12}$$

where the subscript CC denotes coupled channels and the difference (DIF) is given as

$$\chi_{DIF} = \frac{1}{2}(\chi_{EL} - \chi_{EXC})$$

An expansion of equation (12) reveals, as expected, that χ_{EXC} appears only in third-order and higher order terms in $f_{NN}(\mathbf{q})$. As discussed in reference 14, a reasonable approximation to χ_{EXC} is to assume the ground-state density for the excited states. If χ_{EXC} is set equal to χ_{EL} we find

$$f_{CC}^{(2)}(\mathbf{q}) \approx \frac{-ik}{2\pi}\int \exp(-i\mathbf{q}\cdot\mathbf{b})[\exp(i\chi_{EL})\cos\Upsilon - 1]\, d^2b \tag{13}$$

The coherent approximation (ref. 17) is recovered in the limit of small Υ.

By using closure to perform the summations in equation (9), Υ^2 is given as

$$\Upsilon^2(\mathbf{b}) = A_P A_T\left(\frac{1}{2\pi k_{NN}}\right)^2\int d^2q\, d^2q'\, e^{-i\mathbf{q}\cdot\mathbf{b}}\, e^{-i\mathbf{q}'\cdot\mathbf{b}}\, f_{NN}(\mathbf{q})\, f_{NN}(\mathbf{q}')$$

$$\times\left[-A_P A_T\, F^{(1)}(\mathbf{q})\, F^{(1)}(\mathbf{q}')\, G^{(1)}(-\mathbf{q})\, G^{(1)}(-\mathbf{q}') + (A_P - 1)(A_T - 1)\, F^{(2)}(\mathbf{q},\mathbf{q}')\, G^{(2)}(-\mathbf{q},-\mathbf{q}')\right.$$

$$\left.+ (A_T - 1)\, F^{(1)}(\mathbf{q}+\mathbf{q}')\, G^{(2)}(-\mathbf{q},-\mathbf{q}') + (A_P - 1)\, F^{(2)}(\mathbf{q},\mathbf{q}')\, G^{(1)}(-\mathbf{q},-\mathbf{q}')\right] \tag{14}$$

where $F^{(1)}$ and $F^{(2)}$ ($G^{(1)}$ and $G^{(2)}$) are the projectile (target) one- and two-body, ground-state form factors, respectively.

Townsend (ref. 29) has considered Pauli correlation effects between projectile and target nucleons. Here, the first-order elastic phase is written as

$$\chi_{\mathrm{EL}}(\mathbf{b}) = \chi_{\mathrm{DIR}}(\mathbf{b}) - \chi_{\mathrm{EX}}(\mathbf{b}) \tag{15}$$

The direct (DIR) term is written as

$$\chi_{\mathrm{DIR}}(\mathbf{b}) = \frac{A_P A_T}{2\pi k_{\mathrm{NN}}} \int d^2q \; e^{i\mathbf{q}\cdot\mathbf{b}} \; F^{(1)}(-\mathbf{q}) \; G^{(1)}(\mathbf{q}) \; f_{\mathrm{NN}}(\mathbf{q}) \tag{16}$$

and the exchange (EX) term is written as

$$\begin{aligned} \chi_{\mathrm{EX}}(\mathbf{b}) = \frac{A_P A_T}{2\pi k_{\mathrm{NN}}} \int d^2q \; e^{i\mathbf{q}\cdot\mathbf{b}} \; F^{(1)}(-\mathbf{q}) \; G^{(1)}(\mathbf{q}) \\ \times \frac{1}{(2\pi)^2} \int d^2q' \; e^{i\mathbf{q}'\cdot\mathbf{b}} \; f_{\mathrm{NN}}(\mathbf{q}+\mathbf{q}') \; C(\mathbf{q}') \end{aligned} \tag{17}$$

We use the parameterization of f_{NN} as

$$f_{\mathrm{NN}}(\mathbf{q}) = \frac{\sigma(\rho+i)}{4\pi} k_{\mathrm{NN}} \; \exp\left(-\frac{1}{2}Bq^2\right) \tag{18}$$

where k_{NN} is the relative wave number in the two-body system, σ is the two-body scattering cross section, B is the slope parameter, and ρ is the ratio of the real part to the imaginary part of the forward two-body scattering amplitude. Values for the energy-dependent σ, B, and ρ are found in reference 29. The correlation factor is found as

$$C(\mathbf{q}) = \frac{1}{4}\frac{\pi}{d} \; e^{-q^2/4d^2} \tag{19}$$

in reference 29 with $d = 1.85$ fm^{-1}.

The total (TOT) cross section is found from the elastic amplitude by using the optical theorem as follows:

$$\sigma_{\mathrm{TOT}} = \frac{4\pi}{k} \; \mathrm{Im} \; f(\mathbf{q}=0) \tag{20}$$

Equations (13) and (20) show that

$$\begin{aligned} \sigma_{\mathrm{TOT}} = 4\pi \int_0^\infty b \; db \Big\{ 1 - \frac{1}{2}\exp[-\mathrm{Im}(\chi_{\mathrm{EL}} + \Upsilon)] \; \cos[\mathrm{Re}(\chi_{\mathrm{EL}} + \Upsilon)] \\ - \frac{1}{2}\exp[-\mathrm{Im}(\chi_{\mathrm{EL}} - \Upsilon)] \cos[\mathrm{Re}(\chi_{\mathrm{EL}} - \Upsilon)] \Big\} \end{aligned} \tag{21}$$

where Im and Re denote imaginary and real quantities, respectively. The total absorption (ABS) cross section is found by using

$$\sigma_{\mathrm{TOT}} = \sigma_{\mathrm{ABS}} + \sigma_{\mathrm{EL}} \tag{22}$$

where σ_{EL} is the total elastic cross section. Integrating equation (13) by using $d\Omega \approx d^2q/k^2$ and equations (21) and (22) yields

$$\sigma_{\mathrm{ABS}} = 2\pi \int_0^\infty b \; db \Big\{ 1 - \frac{1}{2}\exp(-2 \; \mathrm{Im} \; \chi_{\mathrm{EL}})[\cosh(2 \; \mathrm{Im} \; \Upsilon) + \cos(2 \; \mathrm{Re} \; \Upsilon)] \Big\} \tag{23}$$

2.1. Model Form Factors

The one-body form factor is written in terms of the charge (CH) form factor as

$$F^{(1)}(\mathbf{q}) = F_{\mathrm{CH}}(\mathbf{q})/F_p(\mathbf{q}) \tag{24}$$

where F_p is the proton form factor taken as $e^{-r_p^2 q^2/6}$ with $r_p = 0.86$ fm. For ^{4}He, an excellent fit to the charge form is given by (ref. 30)

$$F_{\mathrm{CH}}(\mathbf{q}) = [1 - (0.316q)^{12}]e^{-(0.681q)^2} \tag{25}$$

The harmonic well model is often used for $A \leq 20$ where the charge form factor is

$$F_{\mathrm{CH}} = (1 - sq^2)e^{-aq^2} \tag{26}$$

and values for parameters s and a are from reference 29. For nuclei where a Woods-Saxon density is appropriate ($A_T \geq 20$),

$$\rho_{\mathrm{CH}}(r) = \frac{\rho_o}{1 + e^{(r-R)/c}} \tag{27}$$

An exact Fourier transform to obtain the charge form factor for a Woods-Saxon density may be found in a series solution (ref. 31)

$$F_{\mathrm{CH}}(q) = \frac{4\pi}{q}\rho_o\ \phi(q) \tag{28}$$

where

$$\phi(q) = \pi Rc\left\{\frac{-\cos(Rq)}{\sinh(\pi cq)} + \frac{\pi c}{R}\,\frac{\sin(Rq)\,\coth(\pi cq)}{\sinh(\pi cq)}\right.$$
$$\left. - \frac{2c}{\pi R}\sum_{m=1}^{\infty}(-1)^m\,\frac{mcq\,\exp(-mR/c)}{\left[(cq)^2 + m^2\right]^2}\right\} \tag{29}$$

The series in equation (29) converges rapidly, and the first three or four terms are accurate for most applications. Values for the parameters c and R are taken from reference 29.

The second-order calculations are difficult because the two-body form factors of the projectile and target must be known. We next consider the Jastrow method of correlated wave functions in order to model the form factors of ^{4}He.

By using a coordinate system unconstrained by the nuclear center of mass, we introduce the model form factors F_M (which are related to the intrinsic form factors) given by

$$F^{(1)}(\mathbf{q}) = \frac{F_M^{(1)}(\mathbf{q})}{F_{\mathrm{CM}}(\mathbf{q})} \tag{30}$$

$$F^{(1)}(\mathbf{q},\mathbf{q}') = \frac{F_M^{(2)}(\mathbf{q},\mathbf{q}')}{F_{\mathrm{CM}}(\mathbf{q}+\mathbf{q}')} \tag{31}$$

with the harmonic oscillator CM correction assumed with

$$F_{\mathrm{CM}}(\mathbf{q}) = \exp\left(\frac{-R^2q^2}{4A}\right) \tag{32}$$

where R is related to the oscillator parameter.

The Jastrow method of correlated basis functions (ref. 32) introduces a correction factor to the wave function calculated in a single-particle potential model in order to take into account the effects of the short-range repulsive part of the nuclear potential on the wave function. The Jastrow-correlated wave function is written as (ref. 32)

$$\Psi_A^c(\mathbf{r}_1 \cdots \mathbf{r}_A) = \Psi_A(\mathbf{r} \cdots \mathbf{r}_A) \prod_{i>j=1}^{A} f(\mathbf{r}_i, \mathbf{r}_j) \tag{33}$$

where Ψ_A represents the Slater determinant for the ground state wave function and the correlation factor $f(\mathbf{r}_i, \mathbf{r}_j)$ is assumed to depend only on the relative separation of $\mathbf{r}_i$ and $\mathbf{r}_j$ and obeys

$$f(\mathbf{r}_i, \mathbf{r}_j) \rightarrow \left\{ \begin{matrix} 0 & (|\mathbf{r}_i - \mathbf{r}_j| \rightarrow 0) \\ 1 & (|\mathbf{r}_i - \mathbf{r}_j| \text{ Large}) \end{matrix} \right\} \tag{34}$$

The two-particle density is given by

$$\rho(\mathbf{r}, \mathbf{r}') = N \int |\Psi_A^c(\mathbf{r}, \mathbf{r}', \mathbf{r}_3, \cdots, \mathbf{r}_A)|^2 d\mathbf{r}_3 \cdots d\mathbf{r}_A \tag{35}$$

where N is the normalization constant.

The Jastrow correlation factor contains up to A-particle correlations. Since our considerations are for two-particle correlations, we consider a low-order approximation to this model (refs. 33 and 34) and write the model two-body density as

$$\rho_M(\mathbf{x}, \mathbf{x}') = N\ \rho_s(\mathbf{x})\ \rho_s(\mathbf{x}')\ |g(\mathbf{x}, \mathbf{x}')|^2 \tag{36}$$

with

$$g(\mathbf{x}, \mathbf{x}') = 1 - e^{-\beta(x-x')^2} \tag{37}$$

where β will determine the correlation length. In equation (36), ρ_s is a single-particle density assumed to be determined by the Slater determinant in equation (33).

By using a single-particle wave function of the form

$$\Psi_s(\mathbf{r}) = \sqrt{N_S}\ e^{-r^2/2R^2} \tag{38}$$

the one- and two-body form factors of ^{4}He are found as (ref. 15)

$$F_M^{(1)}(\mathbf{q}) = \sum_{i=1}^{3} C_i\ e^{-q^2/4v_i} \tag{39}$$

and

$$F_M^{(2)}(\mathbf{q}, \mathbf{q}') = \sum_{i=1}^{3} C_i\ e^{-q^2/4v_i}\ e^{-q'^2/4v_i}\ e^{-d_i\mathbf{q}\cdot\mathbf{q}'} \tag{40}$$

with

$$a_i = \frac{1}{R^2} + \beta_i \tag{41}$$

$$\beta_i = (i-1)\beta \tag{42}$$

$$v_i = a_i - \left(\beta_i^2 / a_i\right) \tag{43}$$

$$d_i = \beta_i / 2 a_i v_i \tag{44}$$

and

$$C_1 = C_T / (a_1 v_1)^{3/2} \tag{45}$$

$$C_2 = -2 C_T / (a_2 v_2)^{3/2} \tag{46}$$

$$C_3 = C_T / (a_3 v_3)^{3/2} \tag{47}$$

where

$$C_T = \left[(a_1 v_1)^{3/2} - 2(a_2 v_2)^{-3/2} + (a_3 v_3)^{-3/2} \right]^{-1} \tag{48}$$

2.2. Results for the Elastic Channel

In figure 1 we show the charge form factor for ^{4}He with the experimental data from references 30 and 35. The solid line is obtained using the model form factor from equation (39) with $1/R^2 = 0.65$ fm^{-2} and $\beta = 2.0$ fm^{-2}, and the dash-dot line comes from the parameterization of equation (25). In figure 2 the two-particle density for ^{4}He is plotted against the relative

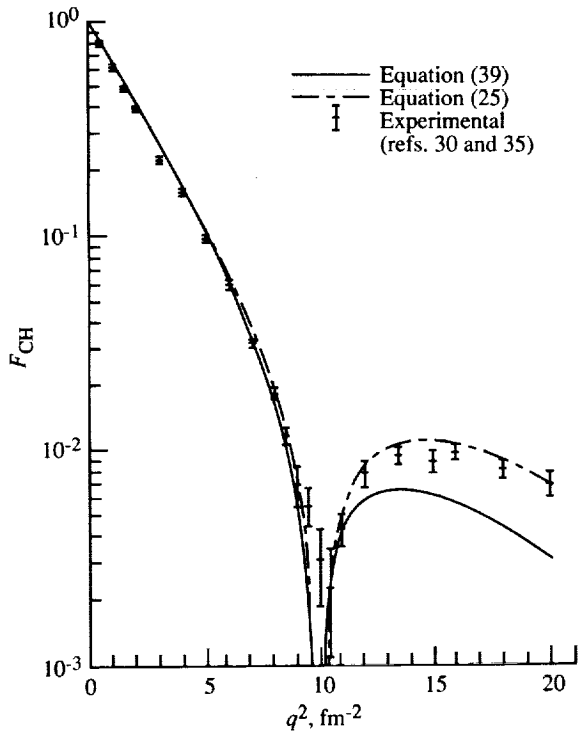

Figure 1. Elastic charge form factor for ^{4}He.

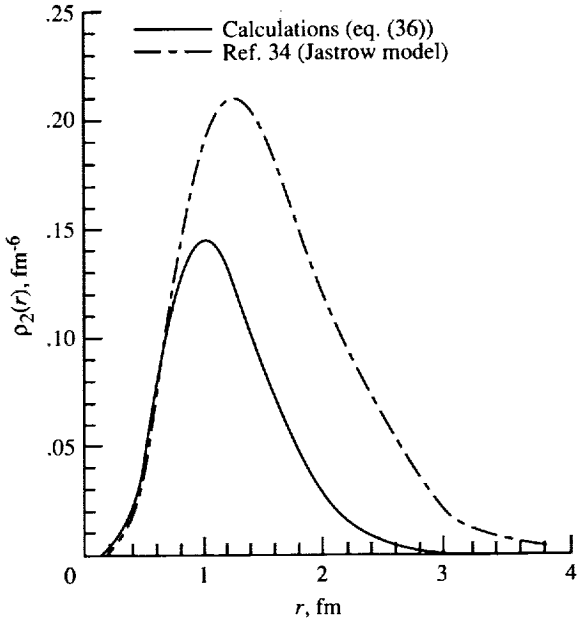

Figure 2. Two-particle density for ^{4}He as function of relative separation distance r.

separation. The solid line is from equation (36), and for comparison a higher order Jastrow calculation from reference 34 is shown as the dash-dot line. Both models lead to about the

same healing distance which is directly related to the position of the minima in the one-body form factor (fig. 1) in our model. In the Jastrow model of reference 34, the CM constraint was neglected which may account for the differences in overall magnitude between the two models.

In figure 3 the elastic cross section for ^{4}He–^{4}He scattering at 635A MeV is shown as a function of the invariant momentum transfer t, where $t = -q^2$. The experimental data are from reference 36. The second-order model shows substantial improvement over the first-order model, especially at the second diffraction maxima where double scattering dominates and leads to excellent agreement with the experiment. In figure 4 a similar comparison is made with the data from reference 37 at 1A GeV.

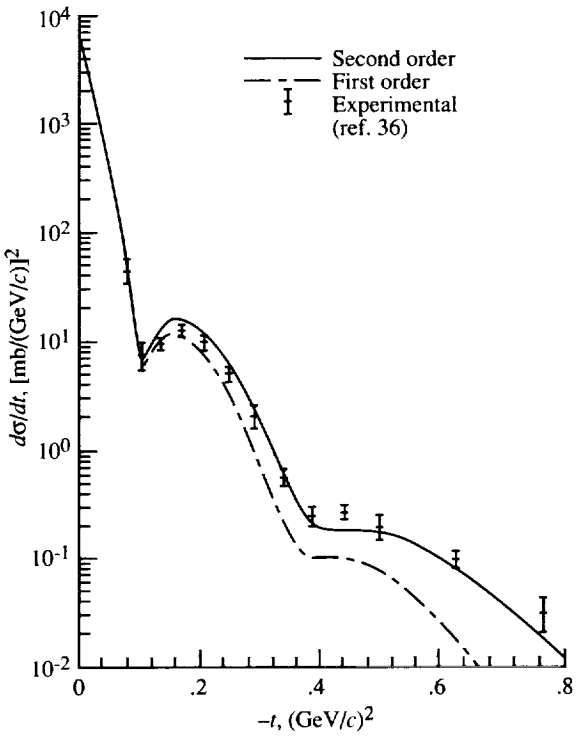

Figure 3. Invariant distribution versus momentum transfer $(-t)$ for α+α elastic scattering at 635A MeV.

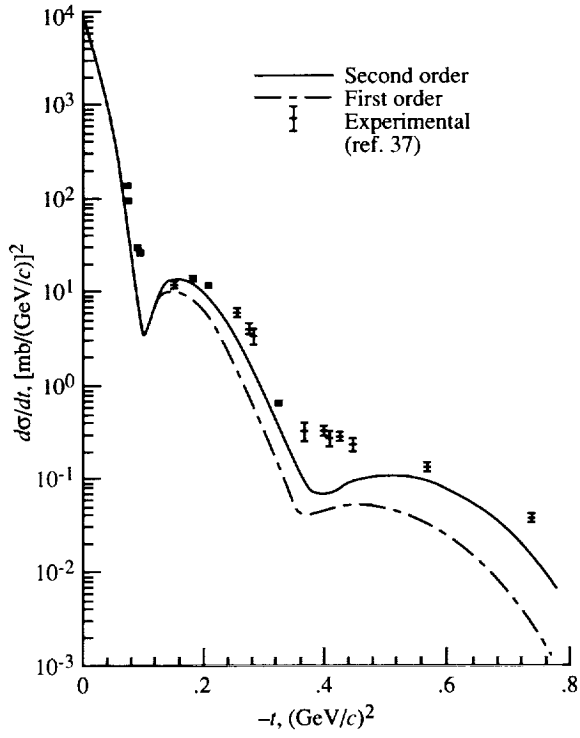

Figure 4. Invariant distribution versus momentum transfer $(-t)$ for α+α elastic scattering at 1A GeV.

Second-order calculations become more difficult for heavier targets if realistic form factors are used since many integrations must be handled numerically in evaluating $\Upsilon(\mathbf{b})$. In figure 5 we show a comparison between first- and second-order calculations for elastic ^{4}He on ^{16}O scattering at 1A GeV with the Jastrow model described above used for ^{16}O in evaluating $\Upsilon(\mathbf{b})$ using the appropriate radii for ^{16}O. Differences between the bordered and coherent model solutions are not substantial, which may be due to our choice of form factors for ^{16}O in $\Upsilon(\mathbf{b})$.

In table 1 the calculations of total and absorption cross sections are compared with experiment for several laboratory (LAB) energies (ref. 38) for α particles reacting with ^{1}H, ^{4}He, and ^{12}C. The second-order calculations are seen to lead to improved agreement with experiment; however, differences between the two solutions are only a few percent. We conclude that the second-order solutions offer improved agreement over the coherent approximation. However, this agreement is already within a few percent for absorption cross sections. Improvements in elastic spectra occur only beyond the forward diffraction peak. Important improvements will likely be found at low energies.

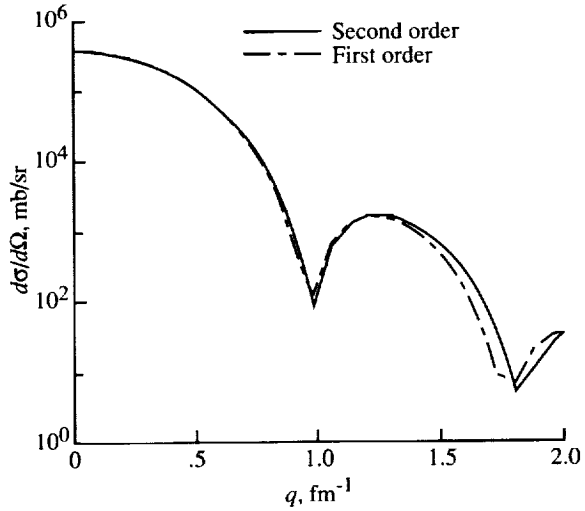

Figure 5. Elastic ^{4}He+^{16}O scattering at 1A GeV.

Table 1. Results for Total and Absorption Cross Sections

T_{LAB}, A MeV	Values of σ_{TOT}, mb, for—			Values of σ_{ABS}, mb, for—		
	First order	Second order	Experiment	First order	Second order	Experiment
			α–p			
870	123	140	143 ± 1.6	94	101	120 ± 6.2
2100	126	142	147 ± 0.4	96	103	111 ± 5.7
			α–α			
870	359	389	390 ± 6.3	244	253	262 ± 18.5
2100	368	397	408 ± 5.5	249	259	276 ± 15
			α–^{12}C			
870	814	829	790 ± 7	520	528	542 ± 16
2100	826	842	835 ± 5	530	536	547 ± 3

3. Quasi-Elastic Scattering

The large energy separation between the ^{4}He ground state and first excited state may lead to a large cross section for quasi-elastic scattering. In the quasi-elastic process the alpha projectile loses energy and receives momentum transfer without suffering a change in mass and, concomitantly, the target nucleus fragments. A significant quasi-elastic (QE) cross section will be important since this process will contribute to the absorption; however, no secondary particles are produced from the projectile in the reaction. The quasi-elastic distributions in momentum and energy transfer are also used to describe the inclusive breakup of light ions (refs. 23 and 24). The QE cross section is evaluated next in the high-energy optical model.

3.1 Scattering Formalism

In treating inelastic scattering we assume that the off-diagonal terms in $\overline{\chi}$, denoted by $\overline{\chi}_o$, are small compared with the diagonal one, $\overline{\chi}_D$, and then we expand $\overline{f}$ from equation (1) in powers of $\overline{\chi}_o$:

$$\overline{f}(\mathbf{q}) = \frac{ik}{2\pi} \int d^2b \; e^{i\mathbf{q}\cdot\mathbf{b}} e^{i\,\overline{\chi}_D(\mathbf{b})} \sum_{m=1} \left\{ \frac{[i\,\overline{\chi}_o(\mathbf{b})]^m}{m!} \right\} \tag{49}$$

We also will make the assumption that the diagonal terms are all represented by the ground-state elastic phase χ. In the remainder of the paper we drop the subscript EL on the elastic phase because it will appear only in a distorted wave, and its meaning should be apparent to the reader. By using equation (3) we sum over target final states X (continuum) to find the inclusive (IN) angular distribution for the projectile when its mass remains unchanged as

$$\frac{d\sigma}{d\Omega}\Big)_{\rm IN} = \frac{k^2}{(2\pi)^2}\int d^2b\; d^2b'\; e^{i\mathbf{q}\cdot(\mathbf{b}-\mathbf{b}')}\;\exp\left\{i[\chi(\mathbf{b})-\chi^+(\mathbf{b}')]\right\}$$
$$\times\sum_{X\neq 0}\sum_{m=1}\frac{1}{(m!)^2}<0_P0_T\left|\left[i\widehat{\chi}(\mathbf{b})\right]^m\right|0_PX>$$
$$\times<X0_P|\left[-i\widehat{\chi}^+(\mathbf{b}')\right]^m|0_P0_T> \tag{50}$$

Equation (50) allows only for a study of the momentum transfer spectra of the projectile. In considering the energy loss of the projectile, energy conservation must be treated. By using continuum states for the target final state, energy conservation leads to

$$\frac{d^2\sigma}{d\Omega\; dE'_P}\Big)_{\rm IN} = \frac{k^2}{(2\pi)^2}\int d^2b\; d^2b'\; e^{i\mathbf{q}\cdot(\mathbf{b}-\mathbf{b}')}\;\exp\left\{i\left[\chi(\mathbf{b})-\chi^+(\mathbf{b}')\right]\right\}\sum_{m=1}^{A_T}W_m(\mathbf{b},\mathbf{b}',\omega) \tag{51}$$

where E'_P is the energy of the projectile in the final state and ω is the energy loss of the projectile. We define

$$W_m(\mathbf{b},\mathbf{b}',\omega)=\frac{1}{(m!)^2}\int\prod_{j=1}^{m}\left[\frac{d\mathbf{k}_j}{(2\pi)^2}\right]\delta(E_f-E_i)<0_P0_T\left|\left[\widehat{\chi}(\mathbf{b})\right]^m\right|0_p\mathbf{k}_j>$$
$$\times<\mathbf{k}_j0_P\left|\left[\widehat{\chi}^+(\mathbf{b}')\right]^m\right|0_P0_T> \tag{52}$$

(refs. 18 and 19) where $\mathbf{k}_j$ is the wave number vector of a knocked-out target nucleon. The functions W_m are next related to the response functions of the target in the cylindrical geometry of the eikonal approximation.

The first collision term is written as

$$W_1(\mathbf{b},\mathbf{b}',\omega)=\frac{A_P^2A_T}{(2\pi k_{\rm NN})^2}\int d^2q\; d^2q'\; e^{i\mathbf{q}\cdot\mathbf{b}}\; e^{-i\mathbf{q}'\cdot\mathbf{b}'}\; F(\mathbf{q})\; F(\mathbf{q}')$$
$$\times f_{\rm NN}(\mathbf{q})\; f^+_{\rm NN}(\mathbf{q}')\int\frac{d^2k}{(2\pi)^2}\;\delta(\omega-E_{\mathbf{k}})\; G_{o\mathbf{k}}(\mathbf{q})\; G^+_{\mathbf{k}o}(\mathbf{q}') \tag{53}$$

where F is the projectile ground-state form factor and $G_{o\mathbf{k}}$ is the target transition form factor. We change variables as

$$\boldsymbol{\alpha}=\frac{1}{2}(\mathbf{q}+\mathbf{q}') \tag{54}$$
$$\boldsymbol{\beta}=\mathbf{q}-\mathbf{q}' \tag{55}$$
$$\mathbf{x}=\mathbf{s}-\mathbf{s}' \tag{56}$$
$$\mathbf{y}=\frac{1}{2}(\mathbf{s}+\mathbf{s}') \tag{57}$$

and also

$$\mathbf{R} = \mathbf{b} - \mathbf{b}' \tag{58}$$

$$\mathbf{S} = \frac{1}{2}(\mathbf{b} + \mathbf{b}') \tag{59}$$

such that

$$W_1(\mathbf{R}, \mathbf{S}, \omega) = \frac{A_P^2 A_T}{(2\pi k_{\rm NN})^2} \int d^2\alpha \; d^2\beta \; e^{i\boldsymbol{\alpha}\cdot\mathbf{R}} \; e^{i\boldsymbol{\beta}\cdot\mathbf{S}} \; A\left(\boldsymbol{\alpha} + \frac{\boldsymbol{\beta}}{2}\right) \; A^+\left(\boldsymbol{\alpha} - \frac{\boldsymbol{\beta}}{2}\right) R_1(\boldsymbol{\alpha}, \boldsymbol{\beta}, \omega) \tag{60}$$

where we have defined

$$A(\mathbf{q}) = F(\mathbf{q}) \; f_{\rm NN}(\mathbf{q}) \tag{61}$$

and the target response function is

$$R_1(\boldsymbol{\alpha}, \boldsymbol{\beta}, \omega) = \int \frac{d\mathbf{k}}{(2\pi)^2} \; \delta(\omega - E_{\mathbf{k}}) \; G_{o\mathbf{k}}\left(\boldsymbol{\alpha} + \frac{\boldsymbol{\beta}}{2}\right) \; G^+_{\mathbf{k}o}\left(\boldsymbol{\alpha} - \frac{\boldsymbol{\beta}}{2}\right) \tag{62}$$

By following Krimm et al. (ref. 39) we can formally treat the delta function in equation (62) by introducing a Fourier transform pair

$$R_1(\boldsymbol{\alpha}, \boldsymbol{\beta}, \omega) = \int \frac{dt}{2\pi} \; e^{i\omega t} \; \widetilde{R}_1(\boldsymbol{\alpha}, \boldsymbol{\beta}, t) \tag{63}$$

$$\widetilde{R}_1(\boldsymbol{\alpha}, \boldsymbol{\beta}, t) = \int d\omega \; e^{-i\omega t} \; R_1(\boldsymbol{\alpha}, \boldsymbol{\beta}, \omega) \tag{64}$$

Then,

$$\widetilde{R}_1(\boldsymbol{\alpha}, \boldsymbol{\beta}, t) = \int \frac{d\mathbf{k}}{(2\pi)^2} \; e^{-iE_{\mathbf{k}}t} \; G_{o\mathbf{k}}\left(\boldsymbol{\alpha} + \frac{\boldsymbol{\beta}}{2}\right) \; G^+_{\mathbf{k}o}\left(\boldsymbol{\alpha} - \frac{\boldsymbol{\beta}}{2}\right) \tag{65}$$

For a nonrelativistic nucleon we have

$$E_{\mathbf{k}} = \frac{\mathbf{k}^2}{2m_N} + \epsilon_{B_1} \tag{66}$$

where ϵ_{B_1} is the binding energy. By assuming plane waves for the target final state in $G_{o\mathbf{k}}$, equation (65) then becomes

$$\widetilde{R}_1(\boldsymbol{\alpha}, \boldsymbol{\beta}, t) = \int \frac{d\mathbf{k}}{(2\pi)^2} \; d\mathbf{x} \; d\mathbf{y} \; e^{-i\epsilon_{B_1}t} \; e^{-i\mathbf{k}^2 t/2m_N} \; e^{i\boldsymbol{\alpha}\cdot\mathbf{x}} \; e^{i\boldsymbol{\beta}\cdot\mathbf{y}} \; e^{i\mathbf{k}\cdot\mathbf{x}}$$
$$\times \Phi\left(\frac{\mathbf{y} + \mathbf{x}}{2}\right) \Phi^+\left(\frac{\mathbf{y} - \mathbf{x}}{2}\right) \tag{67}$$

where Φ is the single-particle wave function of the target ground state. Using equations (67) and (63) gives

$$R_1(\boldsymbol{\alpha}, \boldsymbol{\beta}, \omega) = \left\{ \begin{array}{ll} \frac{m_N}{2\pi} \int d\mathbf{x} \; d\mathbf{y} \; e^{i\boldsymbol{\alpha}\cdot\mathbf{x}} \; e^{i\boldsymbol{\beta}\cdot\mathbf{y}} \; J_o\sqrt{2m_N(\omega - \epsilon_{B_1})x^2} & \\ \quad \times \Phi\left(\mathbf{y} + \frac{\mathbf{x}}{2}\right) \; \Phi^+\left(\mathbf{y} - \frac{\mathbf{x}}{2}\right) & (\omega \geq \epsilon_{B_1}) \\ 0 & (\omega < \epsilon_{B_1}) \end{array} \right\} \tag{68}$$

The higher order collision term is more complicated because of the enumeration of projectile-target intermediate states that can occur. A first approximation is to keep only $1p-1h$ excitations

of the target (one for each inelastic scattering) and assume that the projectile remains in the ground state (coherent approximation).

Using similar coordinate changes as described above, the mth-order collision term is found in the coherent approximation to be

$$W_m(\mathbf{R},\mathbf{S},\omega) = \frac{A_P^{2m} A_T^m}{(m!)^2 (2\pi k_{NN})^{2m}} \int \prod_{j=1}^{m} \Bigg[d^2\alpha_j \; d^2\beta_j \times e^{i\boldsymbol{\alpha}_j\cdot\mathbf{R}} \; e^{i\boldsymbol{\beta}_j\cdot\mathbf{S}} \; A_j\left(\boldsymbol{\alpha}_j + \frac{\boldsymbol{\beta}_j}{2}\right) \; A_j^+\left(\boldsymbol{\alpha}_j - \frac{\boldsymbol{\beta}_j}{2}\right)\Bigg] \times R_m(\boldsymbol{\alpha}_1,\ldots,\boldsymbol{\alpha}_m,\boldsymbol{\beta}_1,\ldots,\boldsymbol{\beta}_m,\omega) \tag{69}$$

where

$$R_m(\boldsymbol{\alpha}_1,\ldots,\boldsymbol{\alpha}_m,\boldsymbol{\beta}_1,\ldots,\boldsymbol{\beta}_m,\omega) = \frac{m_N^m}{(2\pi)^m} \int \prod_{j=1}^{m} \Bigg[d^2x_j \; d^2y_j \; e^{i\boldsymbol{\alpha}_j\cdot\mathbf{x}_j} \; e^{i\boldsymbol{\beta}_j\cdot\mathbf{y}_j} \times \Phi\left(\mathbf{y}_j + \frac{\mathbf{x}_j}{2}\right) \; \Phi^+\left(\mathbf{y}_j - \frac{\mathbf{x}_j}{2}\right)\Bigg] \times \frac{2^{m-1}\left(\omega - \epsilon_{B_m}\right)^{m-1}}{\left[2m_N\left(\omega - \epsilon_{B_m}\right)\sum_{j=1}^{m} x_j^2\right]^{(m-1)/2}} \times J_{m-1}\left[\sqrt{2m_N\left(\omega - \epsilon_{B_m}\right)\sum_{j=1} x_j^2}\right] \tag{70}$$

where $R_m = 0$ for $\omega < \epsilon_{B_m}$. We next consider a simplified representation of the $m > 1$ terms.

By assuming that the target wave functions are forward peaked, we approximate

$$\frac{J_{m-1}\left(\xi_m\sqrt{\sum_{j=1}^{m} x_j^2}\right)}{\left(\xi_m\sqrt{\sum_{j=1}^{m} x_j^2}\right)^{m-1}} \approx \frac{1}{(m-1)!\; 2^{m-1}} \prod_{j=1}^{m} J_o\left[\frac{\xi_m x_j}{2^{(m-1)/2}}\right] + O\left(\xi_m^4 x_j^4\right) \tag{71}$$

where

$$\xi_m = \sqrt{2m_N\left(\omega - \epsilon_{B_m}\right)} \tag{72}$$

such that

$$R_m(\boldsymbol{\alpha}_1,\ldots,\boldsymbol{\alpha}_m,\boldsymbol{\beta}_1,\ldots,\boldsymbol{\beta}_m,\omega) \approx \frac{\left(\omega - \epsilon_{B_m}\right)^{m-1}}{(m-1)!} \prod_{j=1}^{m} R_1\left[\boldsymbol{\alpha}_j,\boldsymbol{\beta}_j,\frac{\xi_m}{2^{(m-1)/2}}\right] \tag{73}$$

and

$$W_m(\mathbf{R},\mathbf{S},\omega) = \frac{\left(\omega - \epsilon_{B_m}\right)^{m-1}}{(m-1)!(m!)^2} \left\{W_1\left[\mathbf{R},\mathbf{S},\frac{\xi_m}{2^{(m-1)/2}}\right]\right\}^m \tag{74}$$

A numerical test of the forward-peaked wave function approximation is discussed below. The energy loss spectrum in a coherent projectile model is given by

$$\frac{d^2\sigma}{d\Omega\, dE'_P}\Big)_{\rm IN} = \frac{k^2}{(2\pi)^2}\int d^2R\, d^2S\, e^{i\mathbf{q}\cdot\mathbf{R}}\, \exp\{i[\chi(\tfrac{\mathbf{S}+\mathbf{R}}{2})-\chi^+(\tfrac{\mathbf{S}-\mathbf{R}}{2})]\}$$

$$\times \sum_{m=1}^{A_T} \frac{(\omega-\epsilon_{Bm})^{m-1}}{(m-1)!(m!)^2}\left\{W_1\left[\mathbf{R},\mathbf{S},\frac{\xi_m}{2^{(m-1)/2}}\right]\right\}^m \tag{75}$$

After angular integration, the energy loss spectrum is found as

$$\frac{d^2\sigma}{dE'_P}\Big)_{\rm IN} = \int d^2S\, e^{-2\ {\rm Im}\ \chi(S)} \sum_{m=1}^{A_T} \frac{(\omega-\epsilon_{Bm})^{m-1}}{(m-1)!(m!)^2}\left\{W_1\left[\mathbf{O},\mathbf{S},\frac{\xi_m}{2^{(m-1)/2}}\right]\right\}^m \tag{76}$$

The coherent approximation assumes that the projectile remains in the ground state throughout the scattering. The leading-order correction to the coherent terms occurs in W_2 and corresponds to the replacement (ref. 40)

$$A_P^4\, F\left(\alpha_1+\frac{\beta_1}{2}\right)\, F\left(\alpha_1-\frac{\beta_1}{2}\right) F\left(\alpha_2+\frac{\beta_2}{2}\right) F\left(\alpha_2-\frac{\beta_2}{2}\right)$$

$$\rightarrow A_P^2\left\{\left[F(2\alpha_1)+(A_P-1)\, F\left(\alpha_1+\frac{\beta_1}{2}\right) F\left(\alpha_1-\frac{\beta_2}{2}\right)\right]\right.$$

$$\left.\times\left[F(2\alpha_2)+(A_P-1)\, F\left(\alpha_2+\frac{\beta_2}{2}\right) F\left(\alpha_2-\frac{\beta_2}{2}\right)\right]\right\} \tag{77}$$

which, physically, represents the projectile dissociating in the intermediate state. Further modifications are necessary when correlation effects not included here are treated.

The distribution in momentum transfer to the projectile nucleus may be obtained from equation (75) after integration over the energy loss. An alternate expression is obtained from equation (49) or (1) through use of closure without regard to energy thresholds for ejecting particles into the continuum given by references 40 and 41. Thus,

$$\frac{d\sigma}{d\Omega}\Big)_{\rm IN} = \left(\frac{k}{2\pi}\right)^2 \int d^2R\, d^2S\, e^{i\mathbf{q}\cdot\mathbf{R}}\, \exp\left\{i\left[\chi\left(\mathbf{S}+\frac{\mathbf{R}}{2}\right)-\chi^+\left(\mathbf{S}-\frac{\mathbf{R}}{2}\right)\right]\right\}\left[e^{\Omega(\mathbf{R},\mathbf{S})}-1\right] \tag{78}$$

with

$$\Omega(\mathbf{R},\mathbf{S}) = \frac{A_P^2 A_T}{(2\pi k_{\rm NN})^2}\int d^2q\, d^2q'\, e^{i\mathbf{q}\cdot\mathbf{b}}\, e^{-i\mathbf{q}\cdot\mathbf{b}'} f_{\rm NN}(\mathbf{q})\, f^+_{\rm NN}(\mathbf{q}')F(\mathbf{q})\, F(\mathbf{q}')\, G(\mathbf{q}-\mathbf{q}') \tag{79}$$

The distributions in momentum transfer obtained from equations (75) and (78) are equivalent if the response function obeys the sum rule

$$\int d\omega \; R_1(\mathbf{q}, \mathbf{q}', \omega) = G(\mathbf{q} - \mathbf{q}') \tag{80}$$

with similar relationships for higher order terms.

An accurate approximation for obtaining numerical results is to expand the elastic coupling phase in equation (75) or (78) as

$$i\left[\chi\left(\frac{\mathbf{S}+\mathbf{R}}{2}\right) - \chi^{+}\left(\frac{\mathbf{S}-\mathbf{R}}{2}\right)\right] = -2 \text{ Im } \chi(\mathbf{S}) - i\mathbf{R}\cdot\nabla_{\mathbf{S}} \text{ Re } \chi(\mathbf{S}) + \ldots \tag{81}$$

with

$$i\mathbf{R}\cdot\nabla_{\mathbf{S}} \; \chi(\mathbf{S}) = -R\cos(\phi_R - \phi_S) \text{ Re } \chi'(\mathbf{S}) \tag{82}$$

where ϕ_R and ϕ_S are azimuthal angles and

$$\chi'(\mathbf{S}) = \frac{A_P A_T}{k_{\text{NN}}} \int_0^\infty q^2 \; dq \; J_1(qS) \; f_{\text{NN}}(q) \; F(q) \; G(q) \tag{83}$$

We then have, for example,

$$\left.\frac{d^2\sigma}{d\Omega \; dE_p}\right)_{\text{IN}} = \frac{k^2}{(2\pi)^2} \int_0^\infty R \; dR \int_0^\infty S \; dS \; e^{-2 \text{ Im } \chi(S)} \; J_o(qR) J_o\left\{R \left[\text{Re } \chi'(S)\right]\right\}$$

$$\times \sum_{m=1}^{A_T} \frac{(\omega - \epsilon_{Bm})^{m-1}}{(m-1)!(m!)^2} \left\{W_1\left[R, S, \frac{\xi_m}{(m-1)/2}\right]\right\}^m \tag{84}$$

The second term in equation (81) physically allows for momentum transfer in elastic scattering and usually makes only a small contribution (ref. 41).

3.2. Shell Model Response Functions

For light nuclei ($A \leq 16$), we use shell model harmonic oscillator wave functions. Thus, for s-shell nucleons,

$$\Phi_s(\mathbf{r}) = \left(\frac{1}{\pi R_T^2}\right)^{3/4} e^{-r^2/2R_T^2} \tag{85}$$

and for p-shell nucleons in a spherical basis with components m,

$$\Phi_{pm}(\mathbf{r}) = \left(\frac{1}{\pi R_T^2}\right)^{3/4} \sqrt{\frac{2}{R_T^2}} \; r_m \; e^{-r^2/2R_T^2} \tag{86}$$

where R_T is the target radii and

$$r_m = \left\{ \begin{array}{ll} \frac{1}{\sqrt{2}}(x \pm iy) & (m = \pm 1) \\ z & (m = 0) \end{array} \right\} \tag{87}$$

The s-shell and p-shell probabilities are given, respectively, by

$$C_s = \frac{4}{A} \tag{88}$$

and

$$C_p = \frac{A-4}{A} \tag{89}$$

From equation (68) the response function is then

$$R_1(\alpha,\beta,\xi_1) = m_N R_T^2 \; e^{-R_T^2\beta^2/4} \; e^{-R_T^2\alpha^2} \; e^{-R_T^2\xi_1^2}$$
$$\times \left\{ \left[2C_s - \frac{C_p}{3} R_T^2\beta^2 + \frac{4}{3} \, C_p R_T^2 \left(\alpha^2 + \xi_1^2\right) \right] I_o \left(2R_T^2\alpha\xi_1\right) \right.$$
$$\left. - \frac{8}{3} C_p R_T^2 \alpha\xi_1 \; I_1 \left(2R_T^2\alpha\xi_1\right) \right\} \tag{90}$$

where I_o and I_1 are modified Bessel functions. Higher order response functions are then approximated by using equations (73) and (90). The collision term W_1 can now be found in analytic fashion, and higher order terms are approximated by using equation (74).

3.3 Results for Quasi-Elastic Scattering

Theoretical calculations for quasi-elastic α–^{4}He scattering at $1A$ GeV are compared with experiment (ref. 42) in figure 6 for several scattering angles. The calculations shown are made with the approximation of equation (75). For consistency we show only the coherent contributions since we have not formulated the corrections for incoherent projectile motion beyond W_2. The multiple scattering structure is apparent with single inelastic collisions dominating at a small momentum transfer and the higher order contributions increasing in importance with q. In figure 6 the second collision term is seen to peak at a smaller energy

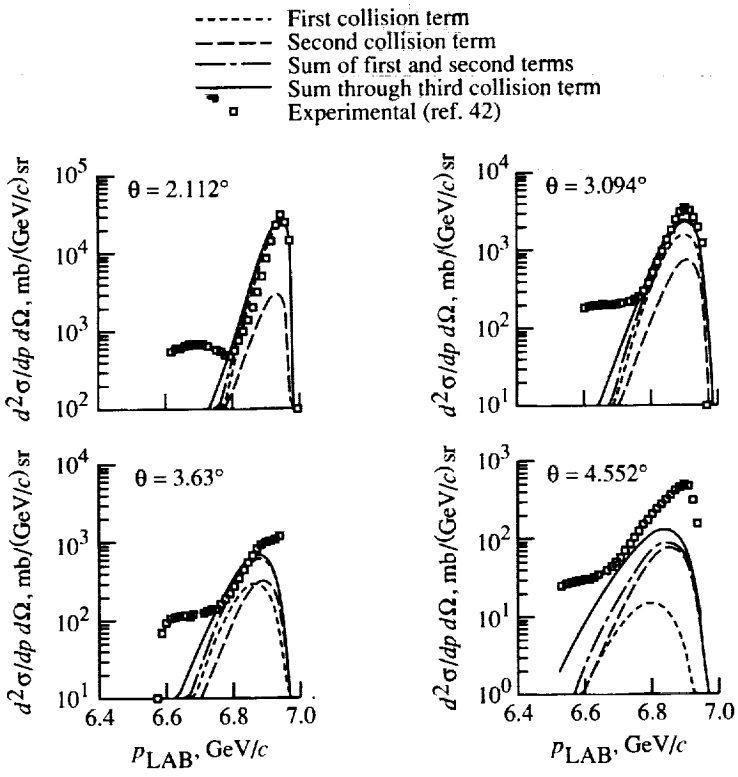

Figure 6. Momentum spectra of α particles in α–^{4}He collisions at $1A$ GeV for scattering angles of 2.112° ($q = 1.31$ fm^{-1}), 3.094° ($q = 1.92$ fm^{-1}), 3.63° ($q = 2.25$ fm^{-1}), and 4.552° ($q = 2.82$ fm^{-1}).

loss than the first term because of the sharing of the total momentum transfer between two scatterings. This effect keeps the position of the theoretical peak in good agreement with the experiment. The strengths of the distributions compare fairly well with experiment except at the largest momentum transfers. This discrepancy grows when calculations are compared with the larger angle data of reference 40 (not shown), and it is attributed, at least partially, to our use of a Gaussian wave function for the ^{4}He ground state.

In figure 7 we illustrate the accuracy of the approximation of equation (73) for the term W_2 for α-α scattering at $\theta = 3.63°$. Incoherent effects are shown to significantly reduce the second collision term. Correlations among projectile nucleons will thus play a role in understanding the quasi-elastic peak.

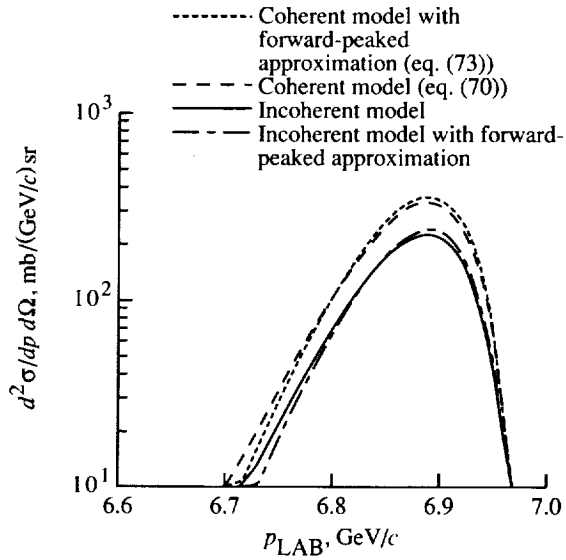

Figure 7. Comparison of calculations of W_2 in various approximations for $\alpha-^4$He scattering at $\theta = 3.63°$. Solid curve is exact incoherent result, dash-dot curve is incoherent result with forward-peaked wave function approximation, dashed-line curve is exact coherent result, and dotted curve is coherent result with forward-peaked wave function approximation.

In figure 8 we show results for quasi-elastic alpha scattering on ^{16}O at 1A GeV for scattering angles of 1° and 4°. The higher order terms are seen to grow in importance with increasing energy loss and momentum transfers.

In figures 9–11 we compare our calculations with the experiments of Ableev et al. (refs. 43 and 44) for the inclusive scattering cross section versus the invariant momentum transfer on ^{12}C, ^{27}Al, and ^{64}Cu targets at 3.6A GeV. The measurements correspond with the sum of the elastic and quasi-elastic cross sections. In the figures the calculations are denoted as elastic scattering using the first-order optical model (dotted line), the quasi-elastic part using equation (78) (dashed line), and total scattering which is the sum of the elastic and quasi-elastic cross sections (solid line). Agreement with experiment is seen to be quite good.

In figure 12 we show predictions for the total quasi-elastic cross section for $\alpha+^{12}$C scattering as a function of laboratory energy. The energy dependence of the cross section follows roughly that of the nuclear absorption cross section and is seen to make up almost 10 percent of the absorption. In figure 13 we show predictions for $\alpha+^{16}$O scattering where similar conclusions apply.

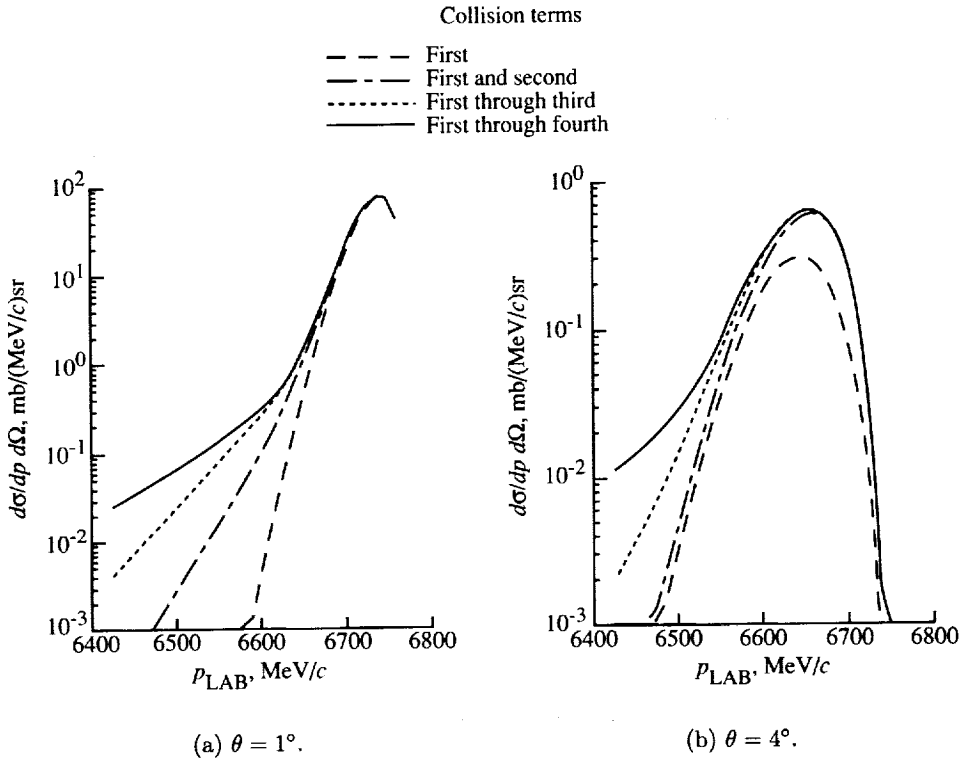

Figure 8. Calculations of quasi-elastic $\alpha - {}^{16}O$ scattering at $1A$ GeV for $\theta = 1°$ and $4°$.

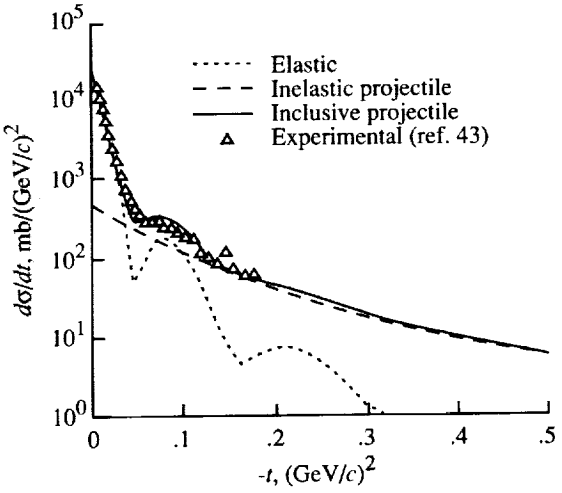

Figure 9. Inclusive ^{4}He+^{12}C scattering distributions at $3.6A$ GeV versus invariant momentum transfer.

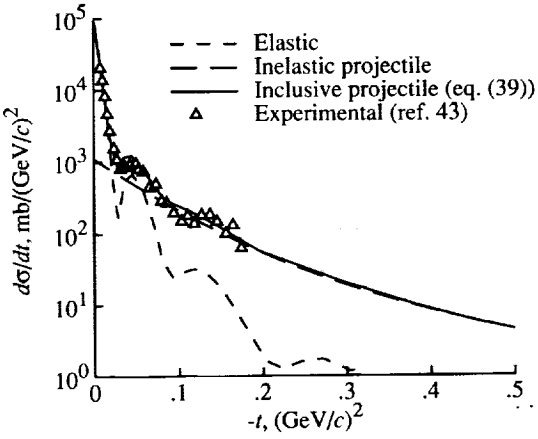

Figure 10. Inclusive ^{4}He+^{27}Al scattering distributions at $3.6A$ GeV versus invariant momentum transfer.

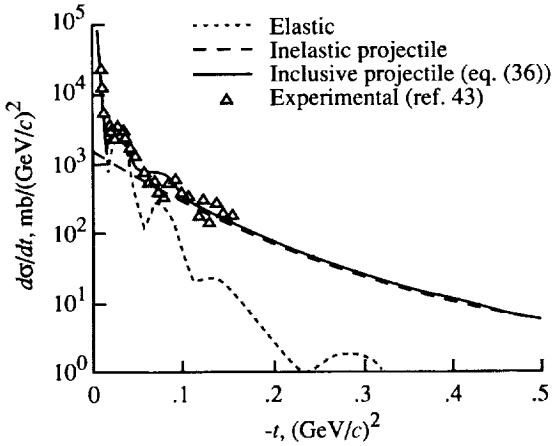

Figure 11. Inclusive ^{4}He+Cu scattering distributions at 3.6A GeV versus invariant momentum transfer.

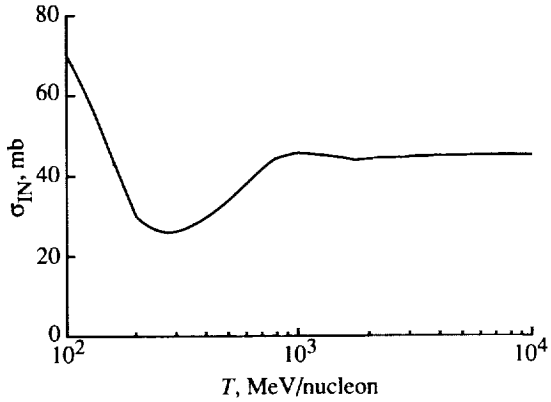

Figure 12. Prediction of quasi-elastic α+^{12}C total cross section versus laboratory energy.

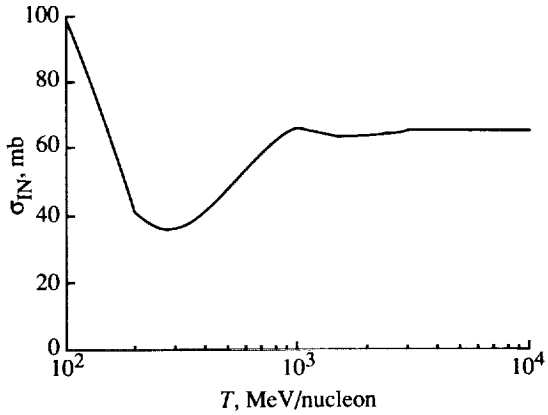

Figure 13. Prediction of quasi-elastic α+^{16}O total cross section versus laboratory energy.

4. Light-Ion Fragmentation on Nuclear Targets

The fragmentation of ^{4}He is somewhat simpler than that of heavier nuclei in that there are only a small number of final states that can occur. These reactions are

$$\alpha + T \rightarrow \begin{cases} {}^3\mathrm{He} + n + X & \text{(91a)} \\ {}^3\mathrm{H} + p + X & \text{(91b)} \\ d + d + X & \text{(91c)} \\ d + n + p + X & \text{(91d)} \\ n + n + p + p + X & \text{(91e)} \end{cases}$$

where X is the final target state. Each of the reactions in equations (91) can occur with or without meson production if sufficient energy is available. The reactions in equations (91) are not exhaustive of the absorption processes; most notable are the compound nuclear and pickup channels that are important at low energies. A model for the two-body dissociation of light ions has been developed (refs. 23, 24, and 45) that describes the first three reactions in equations (91), which we now discuss.

4.1. Two-Body Dissociation Theory

For an inclusive reaction involving the two-body dissociation of the projectile, we write

$$P + T \rightarrow a + b + X \tag{92}$$

where a and b are assumed to be clusters present initially in the projectile and X is the final unobserved target state. We consider the case where a is the observed projectile fragment in the measurement and note that the unobserved target states must be summed over in evaluating the cross section. A summation over possible states of the particle b should also be considered.

By using relativistic kinematics, the transition amplitude ($\mathcal{T}$) for equation (92) is related to the Lorentz invariant momentum distribution for producing the fragment a by

$$E_a \frac{d\sigma}{d\mathbf{p}_a} = E_a \frac{(2\pi)^4}{\beta} \int d\mathbf{p}_b \sum_{m=1}^{A_T} \prod_{j=1}^{m} d\mathbf{p}_j \; \delta(\mathbf{p}_f - \mathbf{p}_i) \; \delta(E_f - E_i) \; |\mathcal{T}_{fi}|^2 \tag{93}$$

where f and i label the final and initial states, respectively, β is the relative projectile-target velocity, and the summation in equation (93) is over the possible configurations of target particles in the final state. A useful approximation to equation (93) is to consider the final target state as an effective particle X and apply energy conservation in an approximate manner. Here we consider an effective three-body problem

$$E_a \frac{d\sigma}{d\mathbf{p}_a} = \frac{(2\pi)^4}{\beta} \int d\Omega_b \mathcal{K} \sum_X |\mathcal{T}_{fi}|^2 \tag{94}$$

where the phase space factor is given by

$$\mathcal{K} = \frac{E_a E_b E_X p_b^2}{p_b(E_b + E_X) + p_a E_b \; \cos(\theta_a + \theta_b)} \tag{95}$$

In equation (94) we are ignoring the mass spectrum of the final target states in imposing energy conservation, and we will assume that $M_X \approx M_T$.

The transition amplitude can be written as a three-body problem of $a - T$, $b - T$, and $a - b$ interactions when rearrangement channels are neglected and with the understanding that all target final and intermediate states must be summed. Using the Faddeev method allows us to consider the multiple scattering series generated by the coupled set of integral equations

$$\hat{\mathcal{T}} = \hat{\mathcal{T}}^a + \hat{\mathcal{T}}^b + \hat{\mathcal{T}}^T \tag{96}$$

with

$$\hat{\mathcal{T}}^a = \hat{T}_{bT} + \hat{T}_{bT} \; G_o(\hat{\mathcal{T}}^b + \hat{\mathcal{T}}^T)$$
$$\hat{\mathcal{T}}^b = \hat{T}_{aT} + \hat{T}_{aT} \; G_o(\hat{\mathcal{T}}^a + \hat{\mathcal{T}}^T)$$
$$\hat{\mathcal{T}}^T = \hat{T}_{ab} + \hat{T}_{ab} \; G_o(\hat{\mathcal{T}}^a + \hat{\mathcal{T}}^b)$$

where $\hat{T}_{aT}$, $\hat{T}_{bT}$, and $\hat{T}_{ab}$ are the "two-body" amplitudes that are the transition operators for aT, bT, or ab scattering, respectively, in the projectile target space and where the Green's function in the impulse approximation is

$$G_o = \left(E - \frac{\mathbf{k}_a^2}{2m_a} - \frac{\mathbf{k}_b^2}{2m_b} - \frac{\mathbf{k}_X^2}{2m_X} + i\eta \right)^{-1} \tag{97}$$

We consider the leading-order corrections to the pole approximation by truncating equation (96) as

$$\widehat{\mathcal{T}} = \left(1 + \widehat{T}_{ab} G_o\right) \left(\widehat{T}_{aT} + \widehat{T}_{bT} + \widehat{T}_{aT} G_o \widehat{T}_{bT} + \widehat{T}_{bT} G_o \widehat{T}_{aT}\right) \tag{98}$$

and replacing $\widehat{T}_{aT}$ and $\widehat{T}_{bT}$ by their on-shell values. However, equation (98) allows for all orders of multiple scattering by assuming the dominance of the ab cluster in the projectile and the fact that ab scatters only after interaction with the target.

The first-order terms of $\mathcal{T}_{fi}$ are shown in figure 14. In figure 14(a) the fragment a is the spectator with the unobserved fragment b interacting with the target. In figure 14(b) the roles of a and b are reversed with b being the spectator. These terms are written as

$$\mathcal{T}_{fi}^{(1)} = \phi(\mathbf{u}_a)\; T_{bX}(\sqrt{s_{bT}}, \mathbf{Q}) + \phi(\mathbf{u}_b)\; T_{aX}(\sqrt{s_{aT}}, \mathbf{Q}) \tag{99}$$

where ϕ is the overlap function representing the virtual projectile decay, $P \to a + b$, $\sqrt{s}$ is the invariant energy for the quasi-scattering of cluster on the target, $\mathbf{Q}$ is the total momentum transfer in the reaction $\mathbf{Q} = \mathbf{p}_T - \mathbf{p}_X$, and

$$\mathbf{u}_a = \mathbf{p}_a - \frac{m_a}{m_p}\mathbf{p}_p \tag{100}$$

$$\mathbf{u}_b = -\mathbf{p}_b + \frac{m_b}{m_p}\mathbf{p}_p = \mathbf{Q} - \mathbf{p}_a \tag{101}$$

From equations (100) and (101) we expect the first term in equation (99) to dominate at small $\mathbf{p}_a$. In equation (99) the amplitudes T_{jT} are half-off shell, where j is either a or b, but are assumed on-shell in a high-energy approximation.

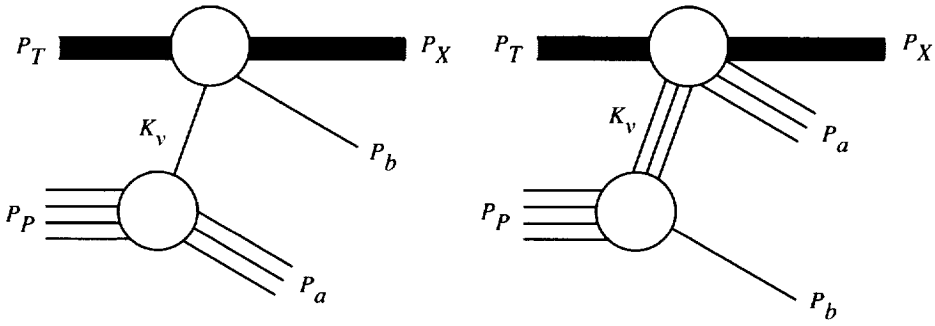

(a) Spectator term. (b) Participant term.

Figure 14. Terms for projectile fragmentation.

In figure 15 corrections for final-state interactions (FSI) between the projectile fragments are shown. The FSI diagram (fig. 15(a)) leads to the integral

$$\mathcal{T}_{fi}^{(1)\prime} = T_{bX}(\sqrt{s_{bT}}, \mathbf{Q}) \int d\mathbf{k}\; \frac{2\mu_{ab}\; \phi\left(\mathbf{k} + \frac{m_a}{m_p}\mathbf{Q}\right) T_{ab}(\mathbf{k}, \mathbf{p}_{ab})}{\mathbf{p}_{ab}^2 - \mathbf{k}^2 + i\epsilon} \tag{102}$$

where $\mathbf{p}_{ab}$ is the relative momentum. We follow references 46–48 and use an off-shell separable $\mathcal{T}$-amplitude for the FSI where the overlap function is used to replace the Yamaguchi potential form factors, thus ensuring orthogonality between the bound and scattering states of a and b.

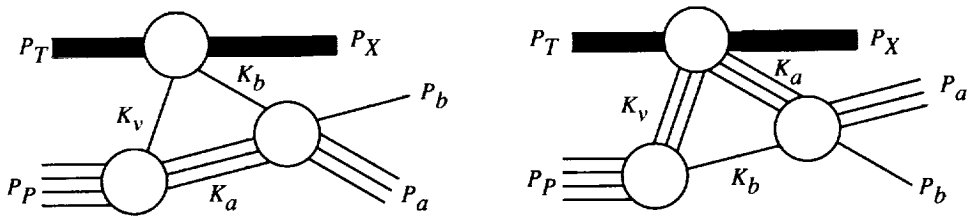

(a) Spectator term.

(b) Participant term.

Figure 15. Terms for final-state interaction.

The higher partial waves are estimated using the Glauber amplitude for ab elastic scattering. The terms in figures 14 and 15 are combined as

$$\widetilde{T}_{fi}^{(1)} = \widetilde{\phi}(\mathbf{u}_a)\ T_{bX}(\sqrt{s_{bT}}, \mathbf{Q}) + \widetilde{\phi}(\mathbf{u}_b)\ T_{aX}(\sqrt{s_{aT}}, \mathbf{Q}) \tag{103}$$

where the distorted overlap function $\widetilde{\phi}$ is defined as

$$\widetilde{\phi}(\mathbf{u}_a) = \phi(\mathbf{u}_a) - \phi(\mathbf{p}_{ab}) \frac{D\left(p_{ab}, \frac{2m_a}{m_p} Q\right)}{D(p_{ab}, O)}$$
$$- \frac{ip_{ab}}{2\pi} \int \sin\theta \cos\theta\ d\theta\ \phi\left(p_{ab}\hat{k} + \frac{m_a}{m_p}\ \mathbf{Q}\right)\ f_{ab}\left(2p_{ab} \sin\frac{\theta}{2}\right) \tag{104}$$

and

$$D(p, q) = -\int d\mathbf{k} \frac{\phi\left(\mathbf{k} + \frac{\mathbf{q}}{2}\right)\ (\alpha^2 + k^2)\ \phi(\mathbf{k})}{p^2 - k^2 + i\eta} \tag{105}$$

where α is related to the $a - b$ separation energy ϵ_s by $\alpha^2 = -2\mu_{ab}\epsilon_s$. The energy-dependent parameters of the two-body amplitudes in f_{ab} are taken from reference 29 with the two-body cross sections allowed to smoothly fall to 0 below 20 MeV such that the s-wave part dominates at low energies.

In equation (103) the decay amplitude ϕ is written in the CM frame; however this amplitude is usually parameterized in the projectile rest frame. We transform to the projectile rest frame using

$$\phi(\mathbf{u}_a) = \left[\frac{E_a(E_p - E_a)E_p}{E'_a(m_p - E'_a)m_p}\right]^{1/2} \phi'(\mathbf{p}'_a) \tag{106}$$

where primed variables represent projectile frame quantities. Using the parameterization

$$\phi'(\mathbf{p}') = \sqrt{N} \sum_{i=1} \frac{a_i}{p'^2 + \alpha_i^2} \tag{107}$$

with $\alpha_1 = \alpha$ and $\sqrt{N}$ being a normalization constant allows the dispersion integral in equation (105) to be evaluated in analytic form. Values for the vertex function parameters are listed in table 2. The overlap probability $|Z|^2$ is also listed in table 2.

In figure 16 we show the rescattering-type correction where both a and b interact with the target. In figure 17 the corrections for FSI to the rescattering are shown. These terms are almost always neglected for composite-composite breakup reactions. For figure 16 we write

$$T_{fi}^{(2)} = 2\mu_{aT} \int d\mathbf{q}_2 \frac{T_{bT}(\mathbf{Q} - \mathbf{q}_2)\ \phi\left(\mathbf{p}_a - \frac{m_a}{m_p}\mathbf{p}_p - \mathbf{Q}\right)\ T_{aT}(\mathbf{q}_2)}{-\mathbf{q}_2^2 - (2\mathbf{p}_{aX} \cdot \mathbf{q}_2) + i\eta} \tag{108}$$

Table 2. Overlap Function Parameters

Projectile	E_s, MeV	α_1, fm^{-1}	α_2, fm^{-1}	α_3, fm^{-1} (a)	$\lvert Z\rvert^2$
$d \to n - p$	2.22	0.232	1.434	0	1.00
$^3\mathrm{H} \to d - n$	7.10	.448	.92	0	.85
$^3\mathrm{He} \to d - p$	7.10	.420	.92	0	.85
$^4\mathrm{He} \to {}^3\mathrm{H} - p$	19.82	.846	1.15	1.65	.60
$^4\mathrm{He} \to {}^4\mathrm{He} - n$	20.58	.863	1.65	1.65	.75
$^4\mathrm{He} \to d - d$	23.85	1.070	1.60	2.50	.50

[a]For $\alpha_3 = 0$: $a_1 = 1$; $a_2 = -1$. For $\alpha_3 \neq 0$: $a_1 = 1$; $a_2 = \frac{-(\alpha_3^2 - \alpha_1^2)}{\alpha_2^2 - \alpha_1^2}$; $a_3 = -a_1 - a_2$.

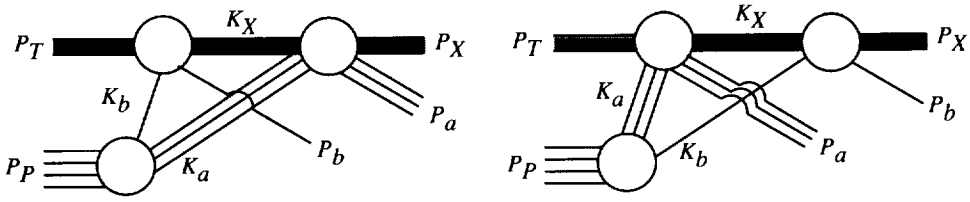

(a) Spectator term. (b) Participant term.

Figure 16. Rescattering corrections.

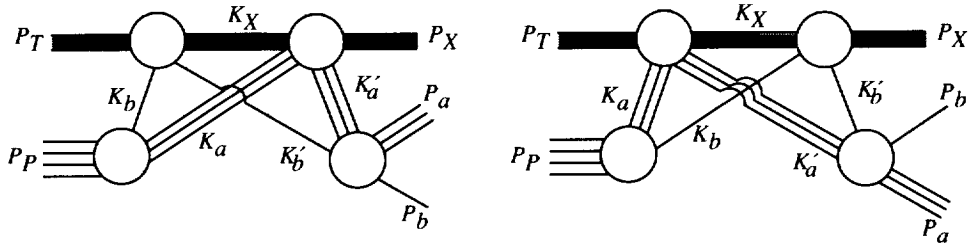

(a) Spectator term. (b) Participant term.

Figure 17. Rescattering corrections with final-state interaction.

with a similar contribution occurring when the roles of a and b are reversed and where $\mathbf{p}_{aX}$ is the relative a and X momentum in the final state.

For figure 17 we find that

$$\mathcal{T}_{fi}^{(2)\prime} = 2\mu_{ab} \int d\mathbf{k}_{ab} \, \frac{T_{ab}(\mathbf{k}_{ab}, \mathbf{p}_{ab})}{\mathbf{p}_{ab}^2 - \mathbf{k}_{ab}^2 + i\epsilon} \times \int d\mathbf{q}_2 \frac{T_{bT}(\mathbf{Q} - \mathbf{q}_2) \; \phi\left(\mathbf{k}_{ab} - \mathbf{q}_2 - \frac{m_a}{m_p}\mathbf{Q}\right) T_{aT}(\mathbf{q}_2)}{\frac{-\mathbf{q}_2^2}{2\mu_{aT}} - \left[\mathbf{q}_2 \cdot \left(\frac{\mathbf{p}_X}{\mu_{PT}} - \frac{\mathbf{k}_{ab}}{m_a}\right)\right] + \frac{1}{2\mu_{ab}}(\mathbf{p}_{ab} - \mathbf{k}_{ab})^2 + i\eta} \tag{109}$$

Equation (109) is considered so that the rescattering corrections can be treated in a consistent manner with the first-order terms because the fragment FSI will occur at a relatively low energy compared with the aT or bT motion. The contribution from equation (109) should be most important for small $\mathbf{p}_{ab}$, and we assume that $p_X \gg p_{ab}$ or k_{ab} in order to reduce the integral to a manageable form. We can then combine equations (108) and (109) in a distorted-wave form as

$$\widetilde{T}_{fi}^{(2)} \approx -\frac{2\pi^2 i\mu_{aT}}{p_{aX}} \int x\, dx\; T_{bT}(\mathbf{Q}-\mathbf{x})\; \widetilde{\widetilde{\phi}}(\mathbf{x},\mathbf{p}_a,\mathbf{Q})\; T_{aT}(\mathbf{x}) \tag{110}$$

where

$$\widetilde{\widetilde{\phi}}(\mathbf{x},\mathbf{p}_a,\mathbf{Q}) = \phi\left(\mathbf{p}_a - \frac{m_a}{m_p}\mathbf{p}_p - \mathbf{x}\right) - \frac{2\mu_{ab}\,\mu_{PT}p_{aX}}{\mu_{aT}p_X} \times \int d\mathbf{k} \frac{\phi\left(\mathbf{k}-\mathbf{x}-\frac{m_a}{m_p}\mathbf{Q}\right)\; T_{ab}(\mathbf{k},\mathbf{p}_{ab})}{p_{ab}^2 - k^2 + i\eta} \tag{111}$$

where $\mathbf{x} = -2p_{aX}\cos\theta_{q_2}\,\hat{q}_2$, and the second term in equation (111) is evaluated similar to that in equation (104). In equation (110) the target final and intermediate states must be considered for inelastic fragmentation.

4.2. Elastic and Inelastic Fragmentation

A convenient way to handle the target state summations is to separate the momentum distribution in equation (94) into elastic and inelastic terms corresponding to the final target state. In elastic fragmentation the target remains in the ground state, and in inelastic fragmentation it remains in the target fragments. This separation is given as

$$E_a\frac{d\sigma}{d\mathbf{p}_a} = E_a\left(\frac{d\sigma}{d\mathbf{p}_a}\right)_{\mathrm{EL}} + E_a\left(\frac{d\sigma}{d\mathbf{p}_a}\right)_{\mathrm{IN}} \tag{112}$$

Using

$$f_{ij} = \frac{-\epsilon_{ij}}{2\pi}\; T_{ij} \tag{113}$$

where $\epsilon_{ij} = E_iE_j/(E_i+E_j)$ and defining the internal momentum distribution Φ of the fragments (in units of $(\mathrm{MeV}/c)^{-3/2}$ where c denotes the speed of light) by $\phi = (2\pi)^{3/2}\Phi$ allows us to write for elastic breakup

$$E_a\left(\frac{d\sigma}{d\mathbf{p}_a}\right)_{\mathrm{EL}} = \frac{1}{\beta}\int d\Omega_p\; \mathcal{K}\; |M_{\mathrm{EL}}|^2 \tag{114}$$

where

$$\begin{aligned} M_{\mathrm{EL}} = {} & \frac{-1}{\epsilon_{bX}}\;\widetilde{\Phi}(\mathbf{u}_a)\; f_{bT}(\mathbf{Q}) - \frac{1}{\epsilon_{aX}}\;\widetilde{\Phi}(\mathbf{u}_b)\; f_{aT}(\mathbf{Q}) \\ & + \frac{\mu_{aT}}{2\epsilon_{aX}\epsilon_{bT}p_{aX}}\int x\, dx\; f_{bT}(\mathbf{Q}-\mathbf{x})\widetilde{\widetilde{\Phi}}(\mathbf{x},\mathbf{p}_a,\mathbf{Q})\; f_{aT}(\mathbf{x}) \\ & + \frac{\mu_{bT}}{2\epsilon_{aT}\epsilon_{bX}p_{bX}}\int y\, dy\; f_{aT}(\mathbf{Q}-\mathbf{y})\widetilde{\widetilde{\Phi}}(\mathbf{y},\mathbf{p}_b,\mathbf{Q})\; f_{bT}(\mathbf{y}) \end{aligned} \tag{115}$$

where f_{aT} is the elastic amplitude that is evaluated in the coherent approximation to the optical model.

For inelastic breakup we have

$$E_a \left(\frac{d\sigma}{d\mathbf{p}_a}\right)_{\rm IN} = \frac{1}{\beta} \int d\Omega_b \mathcal{K} \sum_{X \neq 0} |M_{\rm IN}|^2 \tag{116}$$

where the first-order terms are given as

$$\sum_{X \neq 0} |M^{(1)}_{\rm IN}|^2 = \frac{1}{\epsilon^2_{bX}} |\widetilde{\Phi}(\mathbf{u}_a)|^2 \frac{d\sigma^b}{d\Omega_{\rm IN}}(\mathbf{Q}) + \frac{1}{\epsilon^2_{aX}} |\widetilde{\Phi}(\mathbf{u}_b)|^2 \frac{d\sigma^a}{d\Omega_{\rm IN}}(\mathbf{Q})$$

$$+ \frac{1}{\epsilon_{aX}\epsilon_{bX}} \left\{ \widetilde{\Phi}(\mathbf{u}_a)\, \widetilde{\Phi}^+(\mathbf{u}_b) + \widetilde{\Phi}^+(\mathbf{u}_a)\, \widetilde{\Phi}(\mathbf{u}_b) \right\} \frac{d\sigma^{ab}}{d\Omega_{\rm IN}}(\mathbf{Q}) \tag{117}$$

and with the definitions

$$\frac{d\sigma^a}{d\Omega_{\rm IN}} = \sum_{X \neq 0} | < Xa \mid \widehat{f}_{aT}(\mathbf{Q}) \mid Ta > |^2 \tag{118}$$

and

$$\frac{d\sigma^{ab}}{d\Omega_{\rm IN}} = \sum_{X \neq 0} < aT|\widehat{f}^+_{aT}(\mathbf{Q})|aX >< Xb|\widehat{f}_{bT}(\mathbf{Q})|bT > \tag{119}$$

Equation (118) is just the inclusive distribution for the reaction $a + T \rightarrow a + X$ which corresponds to equation (78) when the optical model is used. The cross section of equation (119) is an interference effect that occurs when there are two virtual projectile clusters available to fragment the target. At high energies we use an on-shell approximation to evaluate equation (119) which is an extension of the optical model result in equation (78). Thus,

$$\frac{d\sigma^{ab}}{d\Omega_{\rm IN}} = \frac{p_{aX} p_{bX}}{(2\pi)^2} \int d^2b\; d^2b'\; e^{i\mathbf{q}\cdot(\mathbf{b}-\mathbf{b}')} \exp\left\{ i\left[\chi_{aT}(\mathbf{b}) - \chi^+_{bT}(\mathbf{b}')\right] \right\} \left[e^{\Omega_{abT}(\mathbf{b},\mathbf{b}')} - 1 \right] \tag{120}$$

where

$$\Omega_{abT} = \frac{A_a A_b A_T}{(2\pi k_{\rm NN})^2} \int d^2q\; d^2q'\; e^{i\mathbf{q}\cdot\mathbf{b}}\; e^{-i\mathbf{q}'\cdot\mathbf{b}'}\; f_{\rm NN}(\mathbf{q}) f^+_{\rm NN}(\mathbf{q}') F_a(\mathbf{q}) F_b(\mathbf{q}')\; G(\mathbf{q}-\mathbf{q}') \tag{121}$$

The higher order inelastic terms are numerous and include terms where both a and b excite the target, only a single cluster excites the target with the second scattering elastically, and the interference terms between the second-order and first-order terms that lead to identical final target states. These terms must include both orderings for a scattering prior to b, and vice versa.

As an example of such processes, double scattering in which only one projectile cluster excites the target nucleus is written as

$$|M_{\rm IN}^{(2)}|^2 = \left(\frac{\mu_{aT}}{2\epsilon_{aX}\epsilon_{bT}p_{aX}}\right)^2 \int x\ dx\ x'\ dx'\ \widetilde{\widetilde{\Phi}}(\mathbf{x},\mathbf{p}_a,\mathbf{Q})\ \widetilde{\widetilde{\Phi}}^{+}(\mathbf{x}',\mathbf{p}_a,\mathbf{Q})$$
$$\times\left[\frac{d\sigma^b}{d\Omega_{\rm EL}}(\mathbf{Q}-\mathbf{x},\mathbf{Q}-\mathbf{x}')\ \frac{d\sigma^a}{d\Omega_{\rm IN}}(\mathbf{x},\mathbf{x}') + \frac{d\sigma^a}{d\Omega_{\rm EL}}(\mathbf{x},\mathbf{x}')\ \frac{d\sigma^b}{d\Omega_{\rm IN}}(\mathbf{Q}-\mathbf{x},\mathbf{Q}-\mathbf{x}')\right]$$
$$+\left(\frac{\mu_{bT}}{2\epsilon_{aT}\epsilon_{bX}p_{bX}}\right)^2 \int y\ dy\ y'dy'\ \widetilde{\widetilde{\Phi}}(\mathbf{y},\mathbf{p}_b,\mathbf{Q})\widetilde{\widetilde{\Phi}}^{+}(\mathbf{y}',\mathbf{p}_b,\mathbf{Q})$$
$$\times\left[\frac{d\sigma^a}{d\Omega_{\rm EL}}(\mathbf{Q}-\mathbf{y},\mathbf{Q}-\mathbf{y}')\frac{d\sigma^b}{d\Omega_{\rm IN}}(\mathbf{y},\mathbf{y}') + \frac{d\sigma^b}{d\Omega_{\rm EL}}(\mathbf{y},\mathbf{y}')\frac{d\sigma}{d\Omega_{\rm IN}}(\mathbf{Q}-\mathbf{y},\mathbf{Q}-\mathbf{y}')\right] \quad (122)$$

where we have defined

$$\frac{d\sigma}{d\Omega_{\rm EL}}(\mathbf{x},\mathbf{x}') = f(\mathbf{x})\ f^{+}(\mathbf{x}') \quad (123)$$

and

$$\frac{d\sigma^j}{d\Omega_{\rm IN}}(\mathbf{x},\mathbf{x}') = \frac{p_{iX}^2}{(2\pi)^2}\int d^2b\ d^2b'\ e^{i\mathbf{x}\cdot\mathbf{b}}\ e^{-i\mathbf{x}'\cdot\mathbf{b}'}\ \exp\left\{i\left[\chi_{jT}(\mathbf{b})-\chi_{jT}^{+}(\mathbf{b}')\right]\right\}\left(e^{\Omega_{jT}(\mathbf{b},\mathbf{b}')}-1\right) \quad (124)$$

4.3. Impulse Terms for Inclusive Deuteron Production

In an inclusive measurement the reactions in equations (91c) and (91d) are not distinguished. The reaction in equation (91d) is more difficult because of its four-body final state with at least three relative motions needed to be considered. Also, the vertex function for ^{4}He $\rightarrow$ *npd* has not been evaluated. We estimate the energy spectra for equation (91b) by considering the impulse terms for this reaction. Higher order scattering terms contribute largely as a normalization correction, and effecting the tails of these spectra will be considered elsewhere.

In figure 18 we show the impulse terms for inclusive deuteron production. These terms are written as

$$\mathcal{T}_{fi} = \phi_d(\mathbf{p}_d)\ T_{dX}(\mathbf{Q}) + \phi_d(\mathbf{p}_d-\mathbf{Q})\ T_{dT}(\mathbf{Q}) + \overline{\phi}_{dn}(\mathbf{p}_d,\mathbf{p}_{dX})\ T_{pX}(\mathbf{Q})$$
$$+\overline{\phi}_{dp}(\mathbf{p}_d,\mathbf{p}_{dX})\ T_{nX}(\overline{Q}) + \overline{\phi}_{np}(\mathbf{p}_d,\mathbf{p}_{np})\ T_{dX}(\mathbf{Q}) \quad (125)$$

where ϕ_d is the $\alpha \rightarrow dd$ vertex and $\overline{\phi}_{ij}$ is the $\alpha \rightarrow dnp$ vertex. We approximate the $\overline{\phi}_{ij}$ vertex function by assuming that the weak binding of the deuteron is such that a correlated neutron-proton pair in ^{4}He closely resembles a deuteron cluster in the ^{4}He ground state. We then assume that

$$\int \overline{\phi}_{dp}(\mathbf{p}_d,\mathbf{p}_{dp})\ d\mathbf{p}_{dp} \approx \phi_d(\mathbf{p}_d) \quad (126)$$

The calculation of the momentum distribution for inclusive deuteron production then closely resembles the evaluation of the impulse terms for the two-body dissociation. We note that the reactions in equations (91c) and (91d) are orthogonal in the projectile Hilbert space.

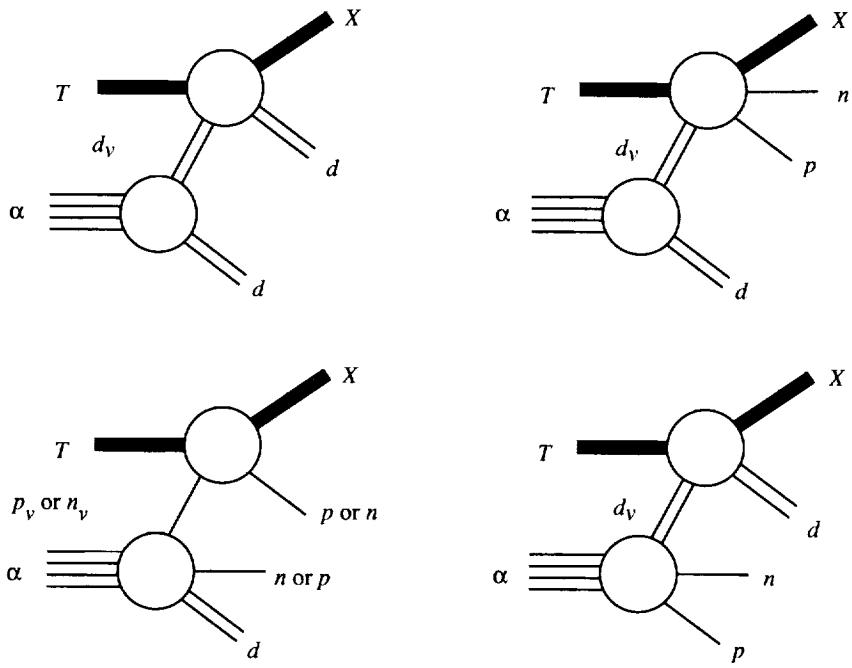

Figure 18. Impulse diagrams for inclusive deuteron production.

4.4. Results for ^{4}He Breakup

We first compare our results with experimental data for ^{1}H targets where inelastic breakup does not occur. In figure 19 the angular distribution for ^{3}He production in 1.02A GeV α particles on ^{1}H collisions is compared with the experimental data of Bizard et al. (ref. 49). Contributions from various breakup terms are labeled on the figure with the total (solid line) agreeing quite well with experiment except at the largest angles.

In table 3 predictions of total production cross sections for ^{3}He and ^{3}H are compared with experimental data from references 49–51. The data from Webber (ref. 50) are preliminary. We note that Webber reports that $\sigma_p < \sigma_{^3\mathrm{H}}$; this cannot be correct because the mechanism for producing ^{3}H will always produce a proton, and several other mechanisms for producing protons exist from equations (91). An error in distinguishing $Z = 1$ fragments is probably at fault. Agreement between theory and experiment is satisfactory. Calculations were made with fixed-energy NN parameters. This ambiguity in on-shell amplitudes will be most important at lower energies (<500 MeV) and for light targets where slope parameters are more important, and thus it should be studied in more detail. The absence of pion production in the model prevents a realistic comparison much higher than 1A GeV for total cross sections. In table 4 predictions are given for the production of ^{3}He from ^{4}He and for deuterons from ^{3}He on several targets. Vertex function parameters for $^3\mathrm{He} \rightarrow pd$ are estimated from Kok and Rinat (ref. 52). For composite targets the higher order terms in equation (98) were not included because of the large computational time required. The higher order terms are expected to increase in importance for heavier targets and lower energies.

Calculations of the longitudinal momentum distribution for triton production at 1.9A GeV are compared with experiment (ref. 22) in figure 20. The dash-dot line is the plane-wave-impulse approximation (PWIA) for proton knockout and clearly underestimates the data. This discrepancy would be only partially resolved by using a wave function with higher momentum components. The short dotted line and the dash-dot line are the impulse terms with FSI for proton and triton exchange, respectively. Note that the final-state interaction causes enhancement in the cross section at large momenta. This conclusion was also found in reference 53 which used a Gaussian wave function and the Glauber model (ref. 54) for

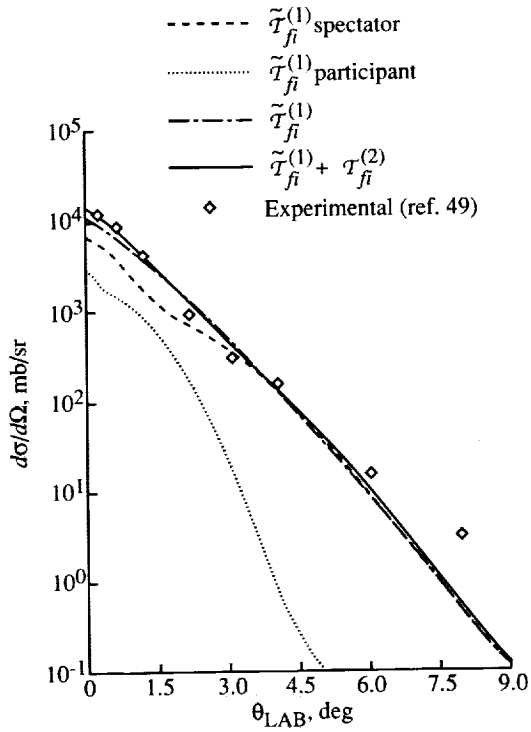

Figure 19. Angular distribution for α+^{1}H $\rightarrow$ ^{3}He at 1.02A GeV.

Table 3. Comparisons of Calculations With Experiments of Webber (ref. 50) for $A = 3$ Fragment Production From ^{4}He

[Calculations are given in parentheses]

(a) α+^{12}C $\rightarrow A_F$

T_{LAB}, A MeV	$\sigma_{^3H}$, mb	$\sigma_{^3He}$, mb
203.3	93.1 ± 9.3 (77.2)	60.4 ± 6.0 (79.3)
377.1	79 ± 7.9 (59.9)	66.9 ± 6.7 (60.9)
519.9	(62.1)	69.4 ± 6.9 (59.8)

(b) α+^{1}H $\rightarrow A_F$

T_{LAB}, A MeV	$\sigma_{^3He}$, mb
377.1	26.3 ± 2.6 (19.5)
519.9	26.4 ± 2.6 (20.8)
1025	24.1 ± 1.9 (22.5)

Table 4. Calculations of Fragmentation Cross Sections for Light-Ion Breakup

(a) α+A_T $\rightarrow$ ^{3}He

T_{LAB}, A MeV	Values of $\sigma_{^3He}$, mb, for—		
	^{12}C	^{16}O	^{27}Al
500	59.8	72.3	96.8
1000	64.1	74.7	100.1

(b) ^{3}He+A_T $\rightarrow$ ^{2}H

T_{LAB}, A MeV	Values of $\sigma_{^2H}$, mb, for—	
	^{16}O	^{27}Al
500	158.0	211.2
1000	128.5	184.0

1.05A GeV α particles. The off-shell s-wave part of the FSI dominates this effect. Including the Glauber amplitude for higher partial waves represents only about a 10-percent correction. The inflection in the dash-dot line near 0.2 GeV/c is caused by the interference between the s-wave and Glauber terms. The solid line and the dashed line in figure 20 are the sum of all terms with and without the effects of interference between the diagrams, respectively. The full calculation provides a good description of the data out to 0.4 GeV/c, but it underestimates at larger values. The effects of interference between diagrams are clearly important.

In figure 21, calculations of the transverse momentum distribution for a beam of energy of 2.09A GeV are compared with the experiment of Anderson et al. (refs. 55 and 56). Triton exchange is seen to contribute only for small values of p_T. The proton knockout term with FSI provides a good representation of the data out to 0.6 GeV/c and falls below the data at higher values. Calculations of pion production in deuteron breakup (ref. 57) suggest that we should expect some contribution from this mechanism at large momentum. In figures 22 and 23, calculations of the transverse momentum distribution at 0.385 and 1.041A GeV, respectively, are shown in comparison with data from references 56 and 57. The total calculation agrees well with the experiment.

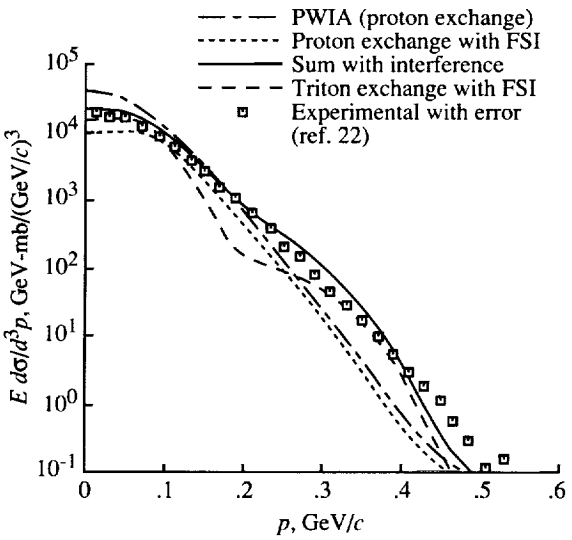

Figure 20. Comparison of calculations of longitudinal momentum distribution for ^{3}H production in $\alpha-^{12}$C collisions at 1.9A GeV with experimental data (ref. 22). Dotted curve is proton exchange term with FSI, dash-dot curve is triton exchange with FSI, dashed-line curve is full calculation neglecting interference effects, and solid curve includes interference.

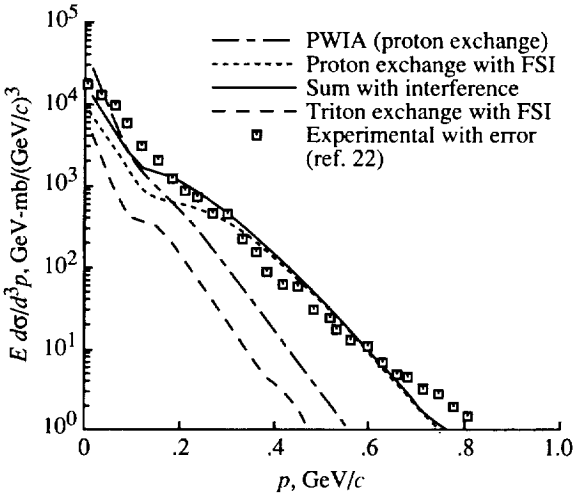

Figure 21. Comparison of calculations of transverse momentum distribution for ^{3}H production in $\alpha-^{12}$C collisions at 2.09A GeV with experimental data.

The calculations in figures 20–23 show that a PWIA extraction of the internal momentum distribution is not possible in inclusive α-nucleus scattering. However, the agreement achieved suggests that a reasonable wave function has been used because several scattering mechanisms contribute and provide a strong constraint on model wave functions. The overlap function employed in our calculations was also found to give good agreement to experiments for pion-induced breakup at 5 GeV/c in reference 48. We also can conclude that a wave function with a minimum below 0.5 GeV/c is not in agreement with the $\alpha-^{12}$C data (refs. 53 and 58). The corrections to the impulse diagrams considered will not hide such a minimum and do not appear in the data. In figure 24, we compare the momentum distribution used here with those extracted in coincidence measurements with 426 MeV electrons (ref. 59) and 500 MeV protons (ref. 21). These experimental distributions will contain distortion effects peculiar to

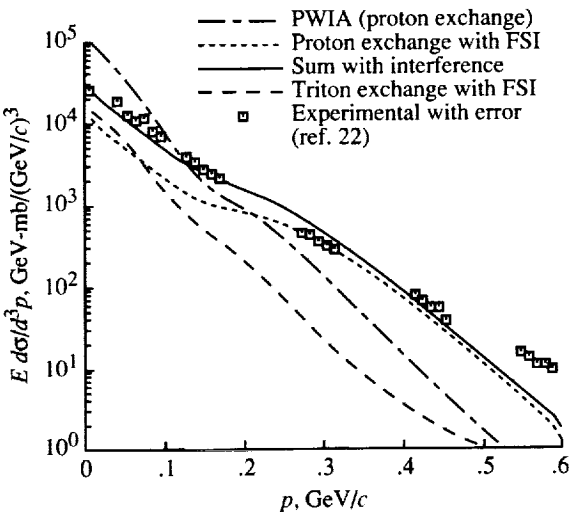

Figure 22. Comparison of calculations of transverse momentum distribution for ^{3}H production in $\alpha-^{12}$C collisions at 0.385A GeV with experimental data.

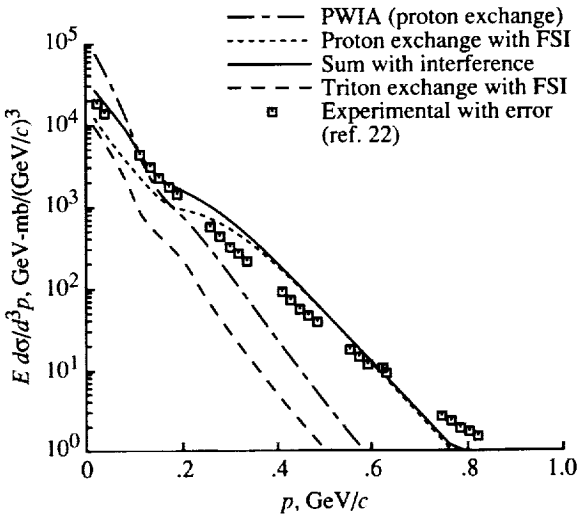

Figure 23. Comparison of calculations of transverse momentum distribution for ^{3}H production in $\alpha-^{12}$C collisions at 1.041A GeV with experimental data.

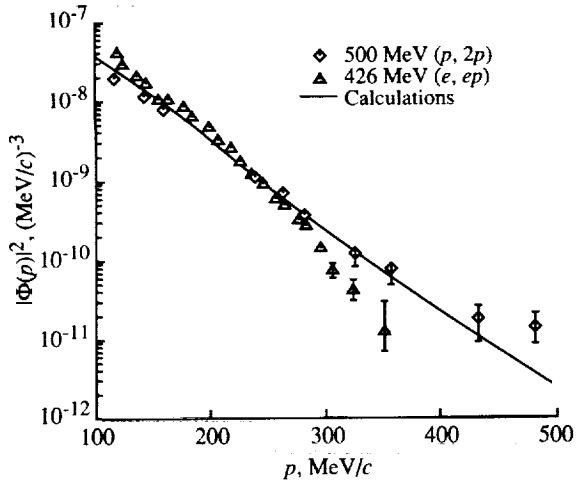

Figure 24. Momentum distribution for ^{3}H in ^{4}He ground state from (e, ep) and $(p, 2p)$ reactions compared with distribution used in calculations.

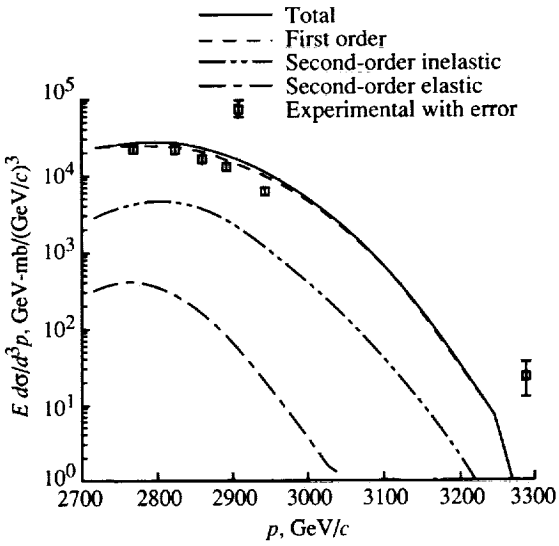

Figure 25. Double-cluster scattering contributions to ^{3}He production on ^{12}C at 385A MeV.

the kinematics employed. Nevertheless, the comparison suggests a common shape out to about 0.4 GeV/c.

The contributions from the double-cluster scattering type of terms (eqs. (109)–(112)) are illustrated in figures 25–26 for ^{3}He production on ^{12}C. The contribution from these rescattering corrections is seen to be small in the longitudinal distribution; however they should increase in importance at larger angles and for lower energies.

The momentum distribution for a deuteron pair in ^{4}He was fit to the Monte Carlo calculations of reference 10 as shown in figure 27. Calculations are shown in figures 28 and 29 with contributions from the various impulse terms shown. A significant contribution is seen for elastic fragmentation at forward angles.

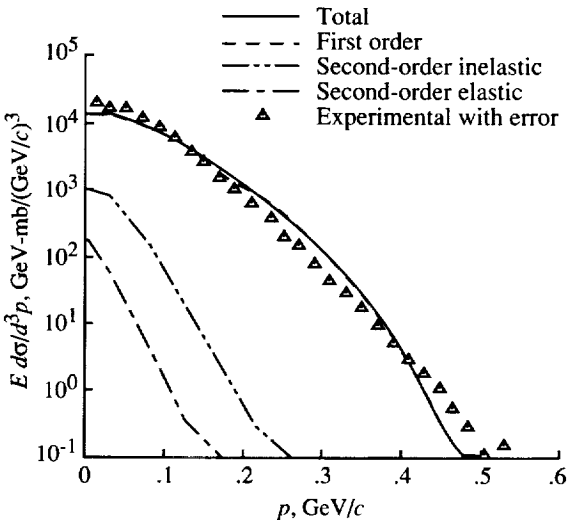

Figure 26. Double-cluster scattering contributions to ^{3}He production on ^{12}C at 1041A MeV.

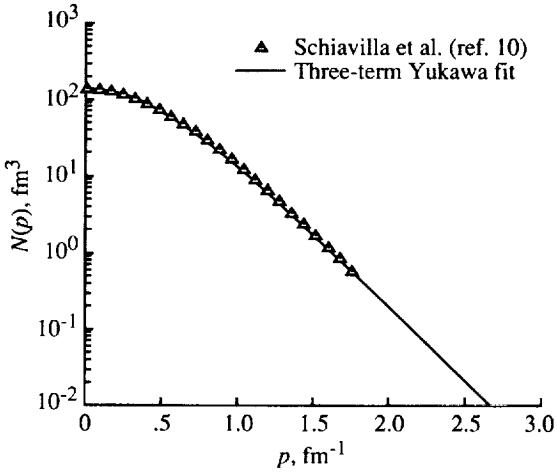

Figure 27. Comparison of momentum distribution for d–d in ^{4}He Monte Carlo calculations of reference 10 with three-term Yukawa fit.

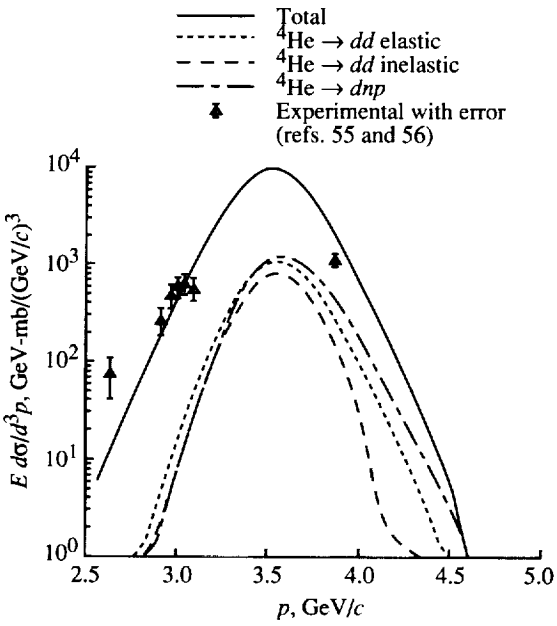

Figure 28. Inclusive d production in α+p reaction at 1.05A GeV.

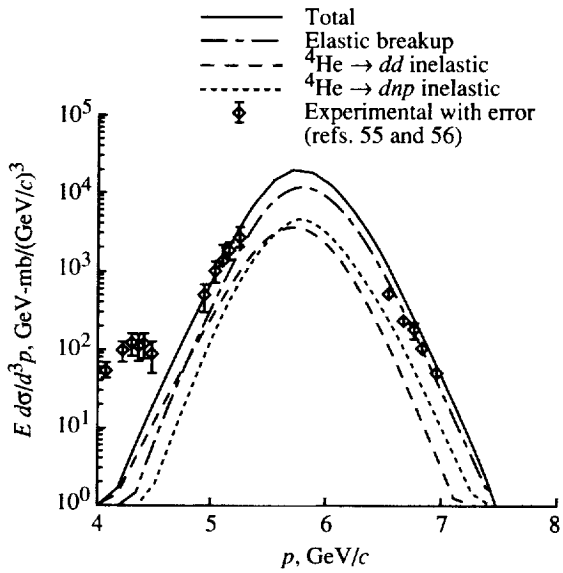

Figure 29. Inclusive d production in α–^{12}C collisions at 2.09A GeV.

Overall, comparing our results with experimental data for ^{4}He fragmentation is encouraging. We can identify several areas that will lead to greater predictive capability. The inclusive scattering model for cluster-target interactions should be extended to include charge exchange which will become important below several hundred MeV/amu. Also, these distributions should be extended to include pion production in order to make predictions at higher energies. Pion absorption on alpha clusters (^{3}He, ^{3}H, and ^{2}H) should then be studied. Final-state interaction effects in ^{2}H production must be included in order to make predictions of total-production cross sections. A first attempt will consider just FSI between two fragments while summing all contributions. Also, off-shell effects in higher partial waves and spin-orbit coupling effects on the FSI should be estimated. The two-body amplitudes employed should be improved for

accuracy at large momentum transfers, especially for ^{1}H targets, and should include nuclear medium effects that will become important at lower energies. Finally, an improved treatment of the many-body phase space for inelastic fragmentation would result from the use of equation (93) with the distribution of equation (75) rather than the approximation of the three-body phase space (eq. (94)) employed here.

5. Parametric Data Base

5.1. Interaction Cross Sections

We next discuss parameterizations of interaction cross sections and energy spectra for alpha particles in common shielding materials. The work of Meyer (ref. 2) gives a complete summary of $\alpha-^1$H cross sections based on measurements up to 1972. Parameterizations of ^{3}H and ^{3}He production on ^{1}H below 300 MeV/amu were discussed in reference 60. An extensive list of earlier references of experiments is given in reference 2. More recent experiments are absorption cross sections between 18 and 48 MeV in reference 61. In reference 62, deuteron production at $1.4A$ GeV was measured with the inclusive deuteron production cross section reported at 30.64 ± 0.62 mb. Also, postdating the compilation by Meyer is the result for $A = 3$ fragments in references 49 and 50. The most important shortcomings of the data base for ^{4}He$-^1$H interactions are high-energy measurements above a few GeV and a complete absence of data for nucleon production cross sections.

By using our theoretical estimates and the existing data, we parameterize the fragmentation cross sections for ^{3}He, ^{3}H, and ^{2}H production on ^{1}H as

$$\sigma_{^3\mathrm{He}} = 42.5\left[\frac{2}{1+e^{(T_{th}-T)/6.8}}-1\right]\left(1-\frac{0.51}{1+6.7e^{-T/34}}\right)^3 \times\left(1+0.36\sqrt{\frac{T}{520}}\right)e^{-(T-780)/2300} \tag{127}$$

$$\sigma_{^3\mathrm{H}} = 15.5\left[\frac{2}{1+e^{(T_{th}-T)/7}}-1\right]\left(1-\frac{0.45}{1+7e^{-T/55}}\right)^3 \times\left(1+1.8\sqrt{\frac{T}{550}}\right)e^{-(T-750)/4500} \tag{128}$$

and

$$\sigma_d = 17\left[\frac{2}{1+e^{(T_{th}-T)/12}}-1\right]\left\{1+\frac{0.21[(T/145)-1]}{1+e^{(145-T)/6}}\right\}e^{-T/3000} \tag{129}$$

where T_{th} is the threshold energy for the breakup reaction listed in table 5 (ref. 63) and T is the kinetic energy in units of A MeV. The low-energy behavior of equation (127) resembles that of reference 60. The pickup cross section is parameterized as

$$\sigma_{\mathrm{PICKUP}} = 48e^{-(T-T_{th})^{1.7/1350}} \tag{130}$$

and contributes to both the inclusive ^{3}He and ^{2}H production cross sections. At low energies the resonance ^{5}Li occurs which is not considered here. The parameterizations are compared with experimental data in figures 30–32. All cross sections are set constant above $3A$ GeV. The energy variations near thresholds and the pion production region are accurately reproduced.

Table 5. Thresholds and Q-Values for $p+^4$He

Reaction	Q, MeV (a)	Threshold, MeV
^{4}He$(p,d)^3$He	−18.354	22.94
^{4}He$(p,2p)^3$He	−19.815	24.77
^{4}He$(p,pn)^3$He	−20.578	25.72
^{4}He$(p,pd)^2$H	−23.848	29.81
^{4}He$(p,ppn)^2$H	−26.072	32.59
^{4}He$(p,ppnn)^1$H	−28.297	35.37

[a]Data taken from references 60 and 63.

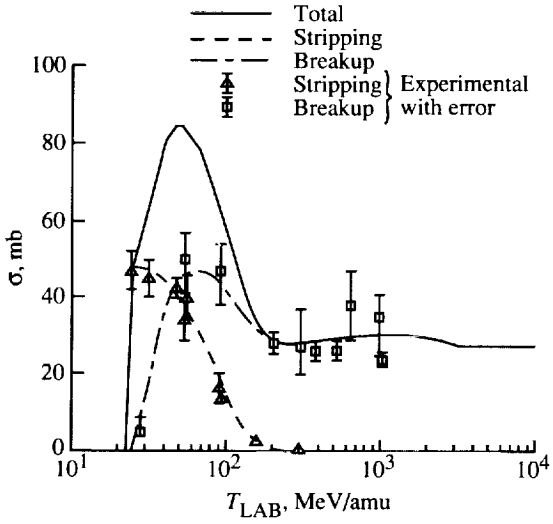

Figure 30. Comparison of parametric model for ^{3}He production in $\alpha-p$ collisions with experimental data.

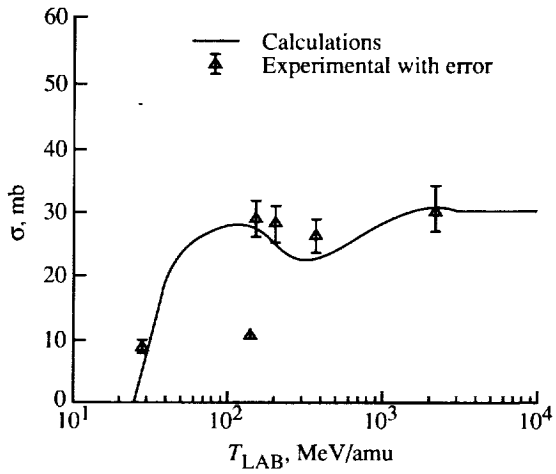

Figure 31. Comparison of parametric model for ^{3}H production in $\alpha-p$ collisions with experimental data.

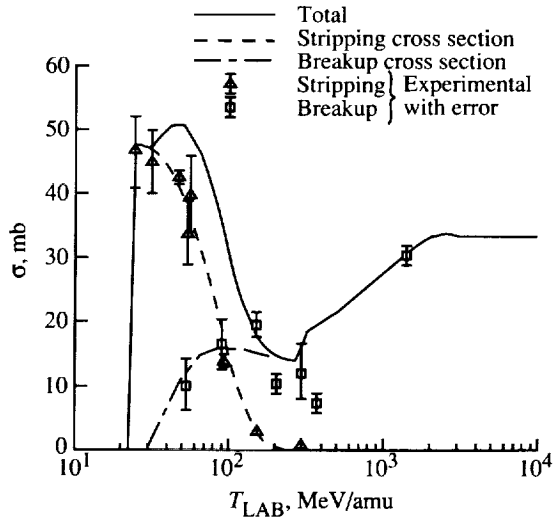

Figure 32. Comparison of parametric model for ^{2}H production in $\alpha-p$ collisions with experimental data.

For the ^{1}H target the absorption (ABS) cross section below 80 MeV is assumed as

$$\sigma_{\mathrm{ABS}} = \sigma_{^3\mathrm{He}} + \sigma_{^3\mathrm{H}} + \sigma_{^2\mathrm{H}} + \sigma_{\mathrm{PICKUP}} \tag{131}$$

Above 80 MeV (and below 80 MeV for $A_T > 1$), the energy-dependent parameterization of Townsend and Wilson (ref. 64) is used which is given by

$$\sigma_{\mathrm{ABS}} = 10\pi\ \beta(E)\ \left[R_{^4\mathrm{He}} + R_{A_T} - 1.26\ \delta(E)\right]^2 \tag{132}$$

where

$$\begin{aligned} \beta(E) &= 1 + \frac{5}{T} \\ \delta(E) &= 0.2 + \frac{1}{A_P} + \frac{1}{A_T} - 0.292e^{-T/792}\ \cos(0.229T^{0.453}) \end{aligned} \tag{133}$$

with a normalization correction of 0.95 used for ^{1}H and the argument of the cosine function given in radians. In equation (132) the nuclear matter radii are used. The absorption cross section for α+^{1}H is shown in figure 33 which presents an excellent reproduction of the experimental data.

The proton and neutron production are expected to rise dramatically above pion production thresholds since two-body collisions will be predominantly inelastic leading to pion absorption in the $A = 3$ or $A = 2$ clusters. Pion production has not been treated in our theoretical considerations. However, the expected rise in proton and neutron cross sections occurs if we simply balance the absorption cross section with channels that do not lead to proton and neutron production, respectively, as shown in figure 34.

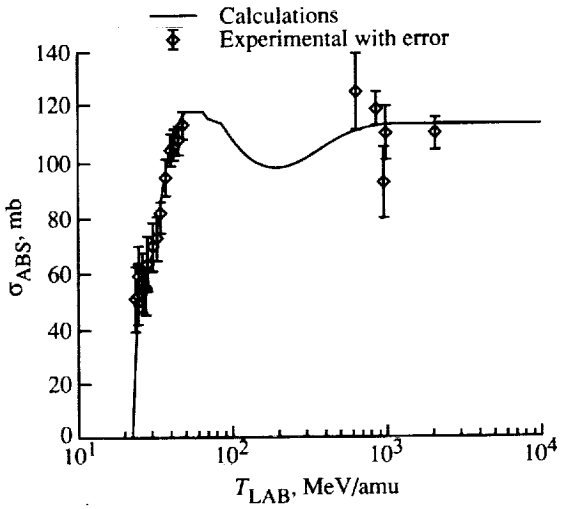

Figure 33. Comparison of parametric model for α+^{1}H absorption cross section with experimental data.

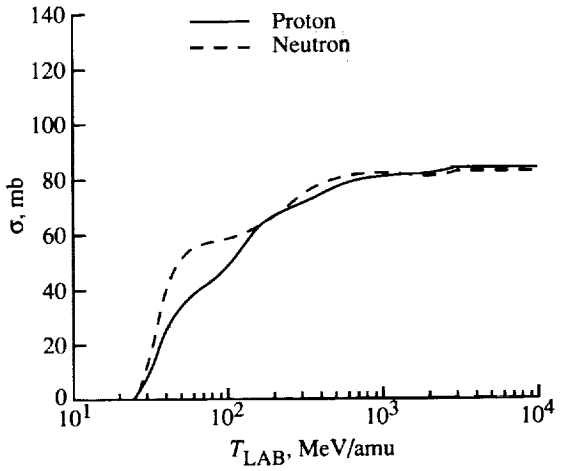

Figure 34. Parametric model predictions for proton production and neutron production in α+^{1}H collisions.

The experimental data base for composite targets is extremely small. A comparison of equation (132) with data for α+^{12}C absorption cross sections is shown in figure 35. Agreement is excellent and previous analyses (ref. 63) suggest similar agreement for other targets. The stripping reactions become more complicated for $A_T > 1$ because several of these channels exist, and stripping or pickup to excited states of the target contributes to the complication. We follow Serber (ref. 25) and assume a surface reaction for nucleon stripping on ^{4}He and then

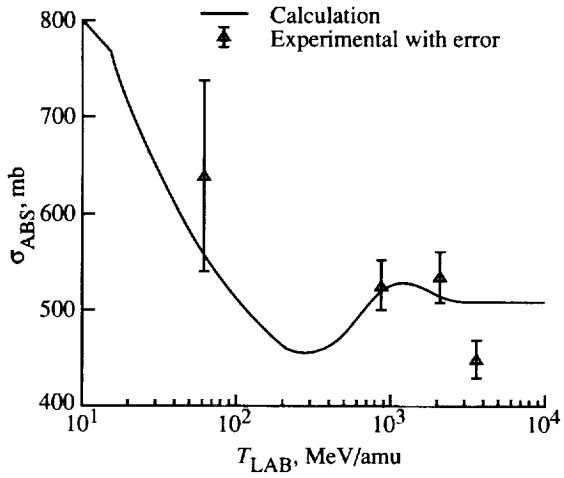

Figure 35. Comparison of parametric model for α+^{12}C absorption cross sections with experimental data.

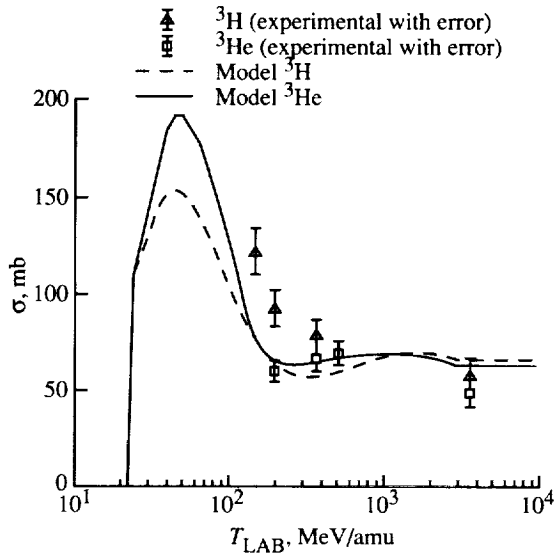

Figure 36. Comparison of fits for ^{3}H and ^{3}He production cross sections with experimental data.

equation (130) is scaled by $A_T^{1/3}$. Since ^{4}He is its own mirror nuclei, we will ignore coulomb effects and assume that equation (130) is used for both ^{3}He and ^{3}H production in stripping reactions. Note that ^{3}H is not produced in stripping on ^{1}H. A slight overestimate may occur because a small contribution from ^{3}He exchange is expected in the reaction α+^{1}H $\rightarrow$ ^{3}He+d. We also ignore any d production in the stripping process for $A_T > 1$. In figure 36 the results for ^{3}H and ^{3}He production on ^{12}C are shown. The fragmentation cross section is scaled as $A_T^{0.31}$ for these fragments. The measurements are from Webber (ref. 50), and the data at 3.6A GeV are from reference 65.

In table 6 we compare parametric fits to secondary yields for charge fragments at 3.6A GeV for several targets as measured in reference 65. The experiment of reference 65 measured only peripheral events with detection angles less than 5°. We expect the measurements of ^{1}H secondaries to be underestimates. The multiplicity for nucleon production from ^{4}He at high energies is between 1 and 1.2 as compared with a value of 2 assumed in existing cosmic ray codes. For ^{2}H we have used a scaling of $A_T^{0.4}$ from our parameterization in equation (129).

Table 6. Comparison of Experimental Fragmentation Cross Sections for ^{4}He Projectiles at 3.6A GeV With Model Fits

[Calculations are given in parentheses]

Fragment	Values of σ_F, mb, for targets[a] of—			
	Li	C	Al	Cu
^{1}H	166 ± 13 (536.6)	227 ± 20 (592.0)	319 ± 34 (823.9)	417 ± 45 (1294.9)
^{2}H	84 ± 15 (68.2)	91 ± 27 (91.2)	113 ± 38 (128.2)	159 ± 45 (184.2)
^{3}H	47 ± 5 (52.7)	58 ± 9 (65.4)	73 ± 20 (84.1)	95 ± 14 (109.9)
^{3}He	48 ± 5 (48.1)	49 ± 8 (59.6)	70 ± 15 (76.7)	95 ± 20 (100.2)

[a]Data were taken from reference 65 which measured only particles in peripheral events ($\theta \leq 5°$).

5.2. Secondary Energy Spectra

The energy spectra of secondary particles is expected to be governed by the internal momentum distribution of the projectile nucleons with a weak dependence on target mass number from dynamic effects. At low energies, kinematic restrictions limit the energy losses possible beyond any restriction provided by the internal momentum distribution. The energy spectra of secondaries from fragmentation is parameterized as

$$\frac{d\sigma}{dE_F} = \sqrt{\frac{2}{\pi}}\,\frac{\sigma_F}{W_F}\,\exp\left[-(T - T_o + \delta_F)^2/2W_F^2\right] \tag{134}$$

where the width W_F, downshift δ_F, and beam energy T_o are in units of A MeV. Values derived from integrating the inclusive momentum distribution of equation (112) over all angles are given in table 7 for several energies and targets. Comparisons of the fit provided by equation (134) with calculations are shown in figures 37–40 and are quite accurate. Note that the internal motion of the projectile constituents leads to fragments produced with velocities higher than the beam velocity.

Table 7. Spectrum Parameters for ^{4}He Fragments

(a) $A = 3$ fragments

Target	δ, A MeV	W, A MeV
500A MeV		
^{1}H	8.5	31.0
^{12}C	9.0	30.0
^{16}O	8.0	30.0
^{27}AL	8.0	30.0
750A MeV		
^{1}H	8.5	35.0
^{12}C	9.0	34.5
^{16}O	8.5	34.0
^{27}AL	8.0	34.0
1000A MeV		
^{1}H	9.0	41.0
^{12}C	9.5	41.0
^{16}O	8.0	42.0
^{27}AL	8.0	42.0

(b) $A = 1$ fragment

Target	δ, A MeV	W, A MeV
500A MeV		
^{1}H	9	58
^{12}C	10	60
^{16}O	10	60
^{27}AL	10	65
750A MeV		
^{1}H	9	77
^{12}C	10	77
^{16}O	10	78
^{27}AL	10	82
1000A MeV		
^{1}H	9	87
^{12}C	10	88
^{16}O	10	90
^{27}AL	10	95

The energy spectrum of the elastically scattered alpha particles is parameterized using the Born term of the optical model expansion that is normalized to the coherent model results (ref. 66). A similar approach is followed to parameterize the quasi-elastic energy spectrum. Assuming a Gaussian density matrix for the target gives (from eq. (76))

$$\frac{d\sigma}{dE_{\alpha'}} = 2m_N z\sigma_{\mathrm{IN}} \exp\left[-2m_N z\left(\omega - \epsilon_{B_1}\right)\right]\ \theta\left(\omega - \epsilon_{B_1}\right) \tag{135}$$

where

$$z = R_T^2 \frac{\frac{R_\alpha^2}{2} + B}{\frac{R_\alpha^2}{2} + B + R_T^2} \tag{136}$$

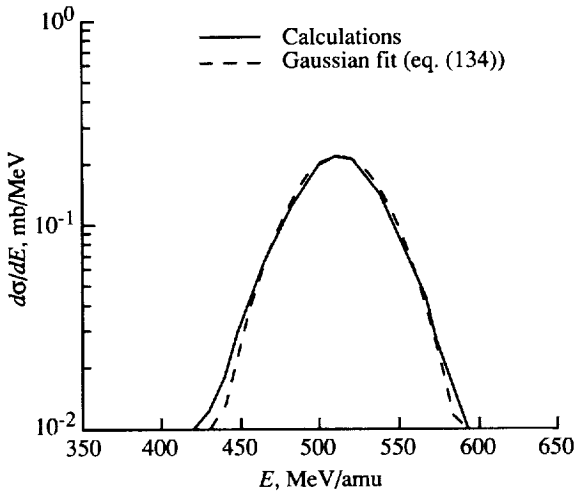

Figure 37. Comparison of calculation of energy spectrum for ^{4}He+^{12}C $\rightarrow$ ^{3}H+X at 520A MeV with Gaussian fit of equation (134).

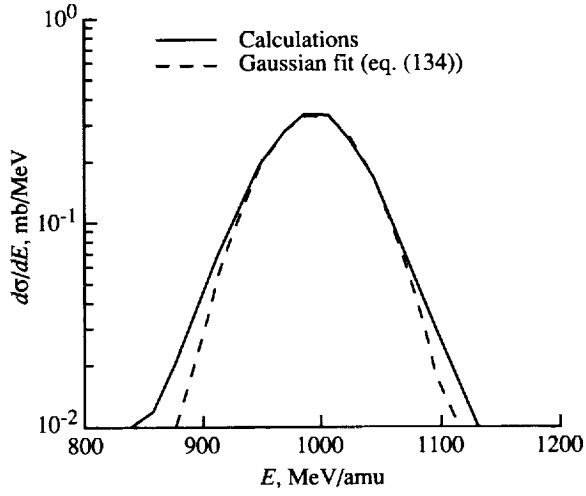

Figure 38. Comparison of calculation of energy spectrum for ^{4}He+^{16}O $\rightarrow$ ^{3}H+X at 1000A MeV with Gaussian fit of equation (134).

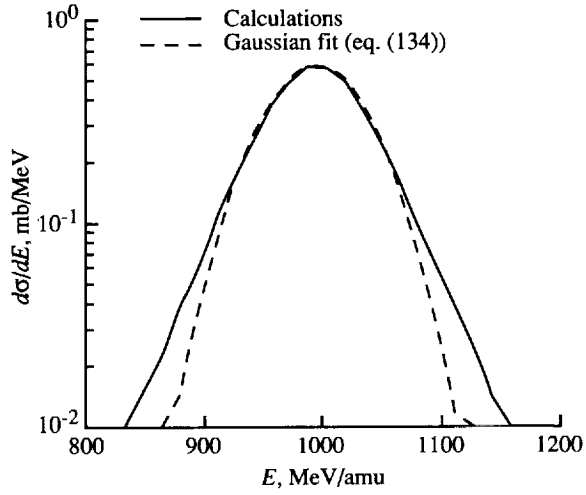

Figure 39. Comparison of calculation of energy spectrum for ^{4}He+^{27}Al $\rightarrow$ ^{3}H+X at 1000A MeV with Gaussian fit of equation (134).

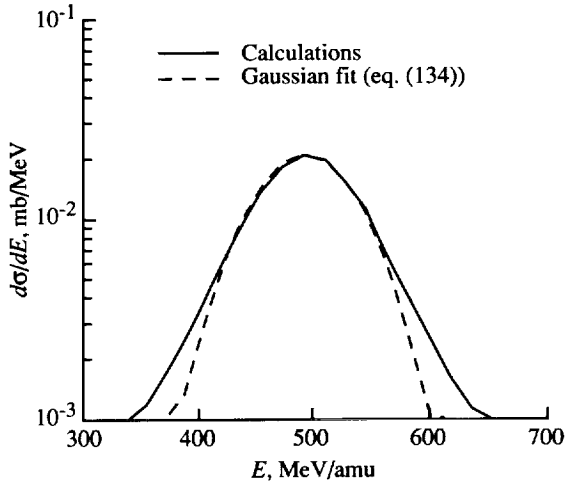

Figure 40. Comparison of calculation of energy spectrum for ^{4}He+^{1}H $\rightarrow$ ^{2}H+X at 500A MeV with Gaussian fit of equation (134).

with R_α and R_T denoting the matter radii of the alpha particle and target, respectively, and B denoting the slope parameter. Equation (135) is expected to underestimate the spectrum at large values of ω because of multiple scattering and perhaps pion production. In figures 41 and 42, illustrations of the fit are shown.

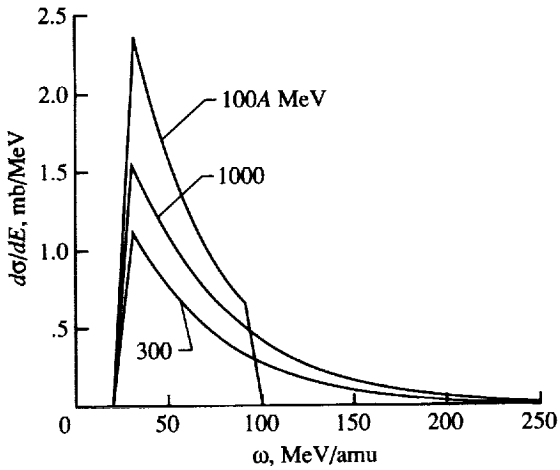

Figure 41. Parametric fits to $\alpha+^{27}\mathrm{Al} \rightarrow \alpha+X$ reaction at 100, 300, 1000A MeV.

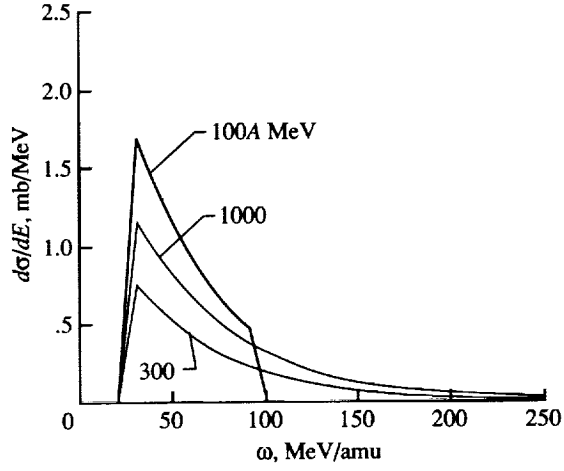

Figure 42. Parametric fits to $\alpha+^{16}\mathrm{O} \rightarrow \alpha+X$ reaction at 100, 300, and 1000A MeV.

6. Concluding Remarks

An overview has been presented of calculations of interaction cross sections for high-energy alpha particles colliding on nuclear targets. Models of elastic, quasi-elastic, and fragmentation channels were described using multiple scattering theory in the impulse approximation. A discussion of future theoretical emphasis was given with pion production at high energies and nuclear medium effects at low energies identified as the principal areas of future work. Extensive comparisons were made with existing experimental data for high-energy alpha particles interacting with nuclear targets, and good agreement was found. Parametric energy-dependent interaction cross sections and energy spectra are presented and discussed.

NASA Langley Research Center
Hampton, VA 23681-0001
December 11, 1992

References

1. Clayton, Donald D.: *Principles of Stellar Evolution and Nucleosynthesis*. McGraw-Hill Book Co., c.1968.

2. Meyer, J. P.: Deuterons and He3 Formation and Destruction in Proton Induced Spallation of Light Nuclei (Z Less Than or Equal to 8). *Astron. & Astrophys. Suppl.*, vol. 7, Dec. 1972, pp. 417–467.

3. Webber, W. R.: *Handbuch der Physik, Band XLVI/2*. Springer-Verlag, 1967.

4. National Council on Radiation Protection and Measurements: *Guidance on Radiation Received in Space Activities*. NCRP Rep. No. 98, July 31, 1989.

5. Machleidt, R.: The Meson Theory of Nuclear Forces and Nuclear Structures. *Advances in Nuclear Physics*, Volume 19, J. W. Negele and Erick Vogt, eds., Plenum Press, c.1989, pp. 189–380.

6. Friar, J. L.; Gibson, B. F.; Lehman, D. R.; and Payne, G. L.: Trinucleon Asymptotic Normalization Constants: Comparison of ^{3}He and ^{3}H. *Phys. Review C*, vol. 37, no. 6, June 1988, pp. 2859–2868.

7. Buck, W. W.; and Gross, Franz: Family of Relativistic Deuteron Wave Functions: *Phys. Review D*, vol. 20, no. 9, Nov. 1, 1979, pp. 2361–2379.

8. Van Meijgaard, E.; and Tjon, J. A.: Theoretical Analysis of Two-Body Electrodisintegration of ^{3}He. *Phys. Review C*, third ser., vol. 42, July–Dec. 1990, pp. 74–95.

9. Carlson, J.; and Pandharipande, V. R.: A Study of Three-Nucleon Interaction in Three- and Four-Body Nuclei. *Nucl. Phys.*, vol. A371, no. 2, Nov. 30, 1981, pp. 301–317.

10. Schiavilla, R.; Pandharipande, V. R.; and Wiringa, R. B.: Momentum Distributions in $A = 3$ and 4 Nuclei. *Nucl. Phys.*, vol. A449, no. 2, Feb. 17, 1986, pp. 219–242.

11. Morita, Hiko; Akaisha, Yoshinori; and Tanaka, Hajime: Realistic Momentum Distributions of the α Particle. *Prog. Theor. Phys.*, vol. 79, no. 4, Apr. 1988, pp. 863–875.

12. Zabolitzky, J. G.; and Ey, W.: Momentum Distributions of Nucleons in Nuclei. *Phys. Lett.*, vol. 76B, no. 5, July 3, 1978, pp. 527–532.

13. Townsend, L. W.; Wilson, J. W.; Cucinotta, F. A.; and Norbury, J. W.: Comparison of Abrasion Model Differences in Heavy Ion Fragmentation: Optical Versus Geometric Models. *Phys. Review*, ser. C, vol. 34, no. 4, Oct. 1986, pp. 1491–1494.

14. Cucinotta, F. A.; Khandelwal, G. S.; Townsend, L. W.; and Wilson, J. W.: Correlations in α-α Scattering and Semi-Classical Optical Models. *Phys. Lett.*, vol. B223, no. 2, June 8, 1989, pp. 127–132.

15. Cucinotta, Francis A.: Theory of Alpha-Nucleus Collisions at High Energies. Ph.D. Thesis, Old Dominion Univ., 1988.

16. Wilson, John W.: Composite Particle Reaction Theory. Ph.D. Diss., College of William and Mary in Virginia, June 1975.

17. Wilson, J. W.; and Townsend, L. W.: An Optical Model for Composite Nuclear Scattering. *Canadian J. Phys.*, vol. 59, no. 11, Nov. 1981, pp. 1569–1576.

18. Cucinotta, Francis A.; Townsend, Lawrence W.; and Wilson, John W.: *Quasi-Elastic Nuclear Scattering at High Energies*. NASA TM-4362, 1992.

19. Cucinotta, Francis A.; Townsend, Lawrence W.; and Wilson, John W.: Multiple Scattering Effects in Quasielastic α–^{4}He Scattering. *Phys. Review C*, vol. 46, no. 4, Oct. 1992, pp. 1451–1456.

20. Perdrisat, C. F.; Swenson, L. W.; Gugelot, P. C.; Boshitz, E. T.; Roberts, W. K.; Vincent, J. S.; and Priest, J. R.: $(p, 2p)$ Reactions at 600 MeV on Deuterium and Helium-4. *Phys. Review*, second ser., vol. 187, no. 4, Nov. 20, 1969, pp. 1201–1209.

21. Frascaria, R.; Roos, P. G.; Morlet, M.; Marty, N.; Willis, A.; Comparat, V.; and Fujiwara, N.: ^{4}He$(p, 2p)^3$H and ^{4}He$(p, pd)^2$H Reactions at 156 MeV. *Phys. Review C*, third ser., vol. 12, no. 1, July 1975, pp. 243–250.

22. Ableev, V. G.; Dshemuchadse, S. V.; Dimitrov, C.; Kobushkin, A. P.; Naumann, B.; Naumann, L.; Nomofilov, A. A.; Penchev, L.; Piskunov, N. M.; Sharov, V. I.; Sitnik, I. M.; Strokovsky, E. A.; Strunov, L. N.; Tesch, S.; and Zaporozhets, S. A.: Proton and Triton Momentum Distributions From ^{4}He Fragmentation at Relativistic Energies. *Few-Body Syst.*, vol. 8, 1990, pp. 137–144.

23. Cucinotta, F. A.; Townsend, Lawrence W.; and Wilson, John W.: Production of ^{3}H at Large Momentum in α-^{12}C Collisions at 2*A* GeV. *Phys. Lett. B*, vol. 282, no. 1,2, May 21, 1992, pp. 1–6.

24. Cucinotta, F. A.; Townsend, L. W.; and Norbury, J. W.: Corrections to Pole Diagrams in ^{4}He Fragmentation at 1 GeV/A. *Bull. American Phys. Soc.*, vol. 34, no. 4, Apr. 1989, p. 1138.

25. Serber, R.: The Production of High Energy Neutrons by Stripping. *Phys. Review*, second ser., vol. 72, no. 11, July 1–Dec. 15, 1947, pp. 1008–1016.

26. Sitenko, A. G.: (O. D. Kocherga, transl.): *Theory of Nuclear Reactions*. World Scientific Publ. Co., c.1990.

27. Guthrie, Miriam P.: *EVAP-4: Another Modification of a Code To Calculate Particle Evaporation From Excited Compound Nuclei*. ORNL-TM-3119, U.S. Atomic Energy Commission, Sept. 10, 1970.

28. Cucinotta, F. A.; Townsend, L. W.; Wilson, J. W.; and Maung, K. M.: Deuteron Production in High-Energy α-Fragmentation. *Bull. American Phys. Soc.*, vol. 36, no. 8, Sept. 1991, p. 2153.

29. Townsend, Lawrence W.: *Harmonic Well Matter Densities and Pauli Correlation Effects in Heavy-Ion Collisions*. NASA TP-2003, 1982.

30. McCarty, J. S.; Sick, I.; and Whitney, R. R.: Electromagnetic Structure of the Helium Isotopes. *Phys. Review C*, third ser., vol. 15, no. 4, Apr. 1977, pp. 1396–1413.

31. Maung, Khin Maung; Deutchman, P. A.; and Royalty, W. D.: Integrals Involving the Three-Parameter Fermi Function. *Canadian J. Phys.*, vol. 67, nos. 2 & 3, Feb.–Mar. 1989, pp. 95–99.

32. Jastrow, Robert: Many-Body Problem With Strong Forces. *Phys. Review*, vol. 98, no. 5, June 1, 1955, pp. 1479–1484.

33. Frullani, Salvatore; and Mougey, Jean: Single-Particle Properties of Nuclei Through (e, e'p) Reactions. *Advances in Nuclear Physics*, Volume 14, J. W. Negele and Erich Vogt, eds., Plenum Press, 1984.

34. Dal Rì, M.; Stringari, S.; and Bohigas, O.: Effects of Short Range Correlations on One- and Two-Body Properties of Nuclei, *Nucl. Phys.*, vol. A376, no. 1, Feb. 22, 1982, pp. 81–93.

35. Frosch, R. F.; McCarthy, J. S.; Rand, R. E.; and Yearian, M. R.: Structure of the He^4 Nucleus From Elastic Electron Scattering. *Phys. Review*, second ser., vol. 160, no. 4, Aug. 20, 1967, pp. 874–879.

36. Berger, J.; Duflo, J.; Goldzahl, L.; Oostens, J.; Plouin, F.; Fabbri, F. L.; Picozza, P.; Satta, L.; Bizard, G.; Lefebvres, F.; Steckmeyer, J. C.; and Legrand, D.: $\alpha\alpha$ Elastic Scattering at 4.32 GeV/c and 5.07 GeV/c. *Nucl. Phys.*, vol. A338, no. 2, Apr. 14, 1980, pp. 421–428.

37. Satta, L.; Duflo, J.; Plouin, F.; Picozza, P.; Goldzahl, L.; Banaigs, J.; Frascaria, R.; Fabbri, F. L.; Codino, A.; Berger, J.; Boivin, M.; and Berthet, P.: Elastic Scattering of α Particles on Light Nuclei at $P_\alpha = 7$ GeV/c. *Phys. Lett.*, vol. 139B, no. 4, May 17, 1984, pp. 263–266.

38. Jaros, J.; Wagner, A.; Anderson, L.; Chamberlain, O.; Fuzesy, R. Z.; Gallup, J.; Gorn, W.; Schroeder, L.; Shannon, S.; Shapiro, G.; and Steiner, H.: Nucleus-Nucleus Total Cross Sections for Light Nuclei at 1.55 and 2.89 GeV/c per Nucleon. *Phys. Review C*, third ser., vol. 18, no. 5, Nov. 1978, pp. 2273–2292.

39. Krimm, H.; Klar, A.; and Pirner, H. J.: Inelastic Scattering of Fast Particles on Nuclei. *Nucl. Phys.*, vol. A367, no. 3, Sept. 14, 1981, pp. 333–357.

40. Cucinotta, Francis A.; Townsend, Lawrence W.; Wilson, John W.; and Khandelwal, Govind S.: *Inclusive Inelastic Scattering of Heavy Ions and Nuclear Correlations*. NASA TP-3026, 1990.

41. Cucinotta, Francis A.; Townsend, Lawrence W.; and Wilson, John W.: Inclusive Inelastic Scattering of Heavy Ions in the Independent Particle Model. *J. Phys. G: Nucl. Particle Phys.*, vol. 18, no. 5, May 1992, pp. 889–901.

42. Banaigs, J.; Berger, J.; Berthet, P.; Bizard, G.; Boivin, M.; De Sanctis, M.; Duflo, J.; Fabbri, F. L.; Frascaria, R.; Goldzahl, L.; Picozza, P.; Plouin, F.; and Satta, L.: Inelastic Scattering of α Particles on Light Nuclei at $P_\alpha = 7.0$ GeV/c. *Phys. Review C*, third ser., vol. 35, no. 4, Apr. 1987, pp. 1416–1424.

43. Ableev, V. G.; Bodyagin, V. A.; Vorob'ev, G. G.; Zaporozhets, S. A.; Nomofilov, A. A.; Piskunov, N. M.; Sitnik, I. M.; Strokovskii, E. A.; Strunov, L. N.; Tarasov, A. V.; Filipkovski, A.; Khristova, I. U.; and Sharov, V. I.: Scattering of 17.9-GeV/c α Particles by C, Al, and Cu Nuclei. *Sov. J. Phys.*, vol. 36, no. 5, Nov. 1982, pp. 698–703.

44. Ableev, V. G.; Dzhemukhadze, S.; Naumann, B.; Nomofilov, A. A.; Piskunov, N. M.; Sharov, V. I.; Shmakov, S. Yu.; Sitnik, I. M.; Strokovsky, E. A.; Strunov, L. N.; Tesch, S.; Uzhinskii, V. V.; and Zaporozhets, S. A.: Diffraction Scattering of Alpha-Particles on Nuclei at 17.9 GeV/c. *Z. Phys. A: Hadrons & Nuclei*, vol. 340, 1991, pp. 191–197.

45. Cucinotta, Francis A.; Townsend, Lawrence W.; Wilson, John W.; and Norbury, John W.: *Corrections to the Participant-Spectator Model of High-Energy Alpha-Particle Fragmentation*. NASA TM-4262, 1991.

46. Kolybasov, V. M.; and Ksenzov, V. G.: Role of Secondary Rescattering in the Reaction $D(\pi^-, \pi^-p)n$ at High Energies. *Sov. J. Nucl. Phys.*, vol. 22, no. 4, July–Dec. 1975, pp. 372–379.

47. Aladashvili, B. S.; Germond, J. F.; Glagolev, V. V.; Nioradze, M. S.; Siemiarczuk, T.; Stepaniak, J.; Streltsov, V. N.; Wilkin, C.; and Zieliński, P.: Final-State Interaction in the High-Energy Proton-Deuteron Break-Up Reaction. *J. Phys. G.*, vol. 3, no. 1, 1977, pp. 7–20.

48. Chevallier, M.; Fäldt, G.; Hallgren, A.; Jonsson, S.; Badelek, B.; Burq, J. P.; Chemarin, M.; Dahlgren, S.; Grafström, P.; Hagberg, E.; Ille, B.; Kullander, S.; Lambert, M.; Nassalski, J.; Querrou, M.; and Vazeille, F.: Quasi-Elastic Pion-Helium Scattering at 5 GeV/c. *Nucl. Phys.*, vol. A343, no. 3, July 21, 1980, pp. 449–467.

49. Bizard, G.; Le Brun, C.; Berger, J.; Duflo, J.; Goldzahl, L.; Plouin, F.; Oostens, J.; Van den Bossche, M.; Vu Hai, L.; Fabbri, F. L.; Picozza, P.; and Satta, L.: ^3He Production in ^4He Fragmentation on Protons at 6.85 GeV/c. *Nucl. Phys.*, vol. A285, no. 3, Aug. 1, 1977, pp. 461–468.

50. Webber, W. R.: New Measurements of the Cross Sections of He-4 Into H-2 and He-3 and Their Implication for H-2 and He-3 Production in Cosmic Rays. *Particle Astrophysics—The NASA Cosmic Ray Program for the 1990s and Beyond*, W. V. Jones, Frank J. Kerr, and Jonathan F. Ormes, eds., American Inst. of Physics, 1990, pp. 294–298.

51. Kozodaev, M. S.; Kulyukin, M. M.; Sulyaev, R. M.; Filippov, A. I.; and Shcherbakov, Yu. A.: Interactions Between 630 Mev Protons and He^4 Nuclei. *Sov. Phys.—JETP*, vol. 11, no. 3, Sept. 1960, pp. 511–516.

52. Kok, L. P.; and Rinat(Reiner): Absolute Normalization of Transfer Amplitudes in the DWBA and Vertex Functions for Light Nuclei. *Nucl. Phys.*, vol. A156, no. 3, Nov. 16, 1970, pp. 593–599.

53. Fujita, T.; and Hüfner, J.: Momentum Distributions After Fragmentation in Nucleus-Nucleus Collisions at High Energy. *Nucl. Phys.*, vol. A343, no. 3, July 21, 1980, pp. 493–510.

54. Glauber, R. J.; and Matthiae, G.: High-Energy Scattering of Protons by Nuclei. *Nucl. Phys.*, vol. B21, no. 1, Aug. 1, 1970, pp. 135-157.

55. Anderson, L.; Brückner, W.; Moeller, E.; Nagamiya, S.; Nissen-Meyer, S.; Schroeder, L.; Shapiro, G.; and Steiner, H.: Inclusive Particle Production at Forward Angles From Collisions of Light Relativistic Nuclei: Nuclear Fragments. *Phys. Review C*, third ser., vol. 28, no. 3, Sept. 1983, pp. 1224–1245.

56. Anderson, L.; Moeller, E.; Nagamiya, S.; Nissen-Meyer, S.; Schroeder, L.; Shapiro, G.; and Steiner, H.: *Inclusive Particle Production at Forward Angles From Collisions of Light Relativistic Nuclei, Part III: Data Tables.* LBL-14330 (Contract DE-AC03-76SF00098), Dep. of Physics, Univ. of California, May 1982.

57. Azhgirey, L. S.; Ignatenko, M. A.; Kuznetsov, A. S.; Razin, S. V.; Stoletov, G. D.; Vzorov, I. K.; Yudin, N. P.; and Zhmyrov, V. N.: Fragmentation of 9 GeV/c Deuterons in the Region of Proton Transverse Momenta of 0.5-1 GeV/c and the Deuteron Wave Function at Small Distances. *Nucl. Phys.*, vol. A528, nos. 3, 4, June 17, 24, 1991, pp. 621–646.

58. Lim, T. K.: Normalization of the p-^{3}H and n-^{3}He Tails of ^{4}He and the ^{4}He Charge Form Factor. *Phys. Lett.*, vol. 44B, no. 4, May 14, 1973, pp. 341–342.

59. Van den Brand, J. F. J.; Blok, H. P.; Ent, R.; Jans, E.; Kramer, G. J.; Lanen, J. B. J. M.; Lapikás, L.; Quint, E. N. M.; Van der Steenhoven, G.; de Witt Huberts, P. K. A.: Electrodisintegration of ^{4}He Studied With the Reaction ^{4}He(e,e'p)^{3}H. *Phys. Review Lett.*, vol. 60, no. 20, May 16, 1988, pp. 2006–2009.

60. Bildsten, Lars; Wasserman, Ira; and Salpeter, Edwin E.: A Semi-Classical Model for Breakup Reactions of Light Nuclei: ^{4}He(p,pn)^{3}He. *Nucl. Phys.*, vol. A516, no. 1, Sept. 17, 1990, pp. 77–107.

61. Sourkes, A. M.; Houdayer, A.; Van Oers, W. T. H.; Carlson, R. F.; and Brown, Ronald E.: Total Reaction Cross Section for Protons on ^{3}He and ^{4}He Between 18 and 48 MeV. *Phys. Review C*, third ser., vol. 13, no. 2, Feb. 1976, pp. 451–460.

62. Aladashvili, B. S.; Bánó, M.; Braun, H.; Gerber, J. P.; Glagolev, V. V.; Gorbunov, A. N.; Hlaváčová, J.; Juillot, P.; Khairetdinov, K. U.; Lebedev, R. M.; Martinská, G.; Menteshashvili, Z. R.; Michalon, A.; Mirianashvili, D. G.; Nioradze, M. S.; Patočka, J.; Seman, M.; Sobszak, T.; Stepaniak, J.; Streltsov, V. N.; Šándor, L.; Urban, J.; Zhuravleva, L. I.; and Futó, A.: Production of Deuterons in a ^{4}He$-p$ Interaction at 8.6 GeV/c. *Acta Phys. Slov*, vol. 31, no. 1, 1981, pp. 29–37.

63. Fiarman, S.; and Meyerhof, W. E.: Energy Levels of Light Nuclei A = 4. *Nucl. Phys.*, vol. A206, no. 1, May 14, 1973, pp. 1–64.

64. Townsend, L. W.; and Wilson, J. W.: Energy-Dependent Parameterization of Heavy-Ion Absorption Cross Sections. *Radiat. Res.*, vol. 106, 1986, pp. 283–287.

65. Abdurakhimov, A. Kh.; Anikina, M. Kh.; Buttsev, V. S.; Chikovani, L. D.; Chkhaidze, L. V.; et al.: A Study of Pion Production in 4.5 (GeV/c)/Nucleon ^{4}He Interactions With Nuclear Targets. *Nucl. Phys.*, vol. A362, no. 2, June 8, 1981, pp. 376–390.

66. Wilson, John W.; Townsend, Lawrence W.; Schimmerling, Walter; Khandelwal, Govind S.; Khan, Ferdous; Nealy, John E.; Cucinotta, Francis A.; Simonsen, Lisa C.; Shinn, Judy L.; and Norbury, John W.: *Transport Methods and Interactions for Space Radiations.* NASA RP-1257, 1991.

REPORT DOCUMENTATION PAGE

Form Approved
OMB No. 0704-0188

1. AGENCY USE ONLY *(Leave blank)*	2. REPORT DATE	3. REPORT TYPE AND DATES COVERED
	April 1993	Technical Paper

4. TITLE AND SUBTITLE
Description of Alpha-Nucleus Interaction Cross Sections for Cosmic Ray Shielding Studies

5. FUNDING NUMBERS
WU 593-42-21-01

6. AUTHOR(S)
Francis A. Cucinotta, Lawrence W. Townsend, and John W. Wilson

7. PERFORMING ORGANIZATION NAME(S) AND ADDRESS(ES)
NASA Langley Research Center
Hampton, VA 23681-0001

8. PERFORMING ORGANIZATION REPORT NUMBER
L-17139

9. SPONSORING/MONITORING AGENCY NAME(S) AND ADDRESS(ES)
National Aeronautics and Space Administration
Washington, DC 20546-0001

10. SPONSORING/MONITORING AGENCY REPORT NUMBER
NASA TP-3285

11. SUPPLEMENTARY NOTES

12a. DISTRIBUTION/AVAILABILITY STATEMENT
Unclassified–Unlimited

Subject Category 73

12b. DISTRIBUTION CODE

13. ABSTRACT *(Maximum 200 words)*
Nuclear interactions of high-energy alpha particles with target nuclei important for cosmic ray studies are discussed. Models for elastic, quasi-elastic, and breakup reactions are presented and compared with experimental data. Energy-dependent interaction cross sections and secondary spectra are presented based on theoretical models and the limited experimental data base.

14. SUBJECT TERMS
Nuclear fragmentation; Multiple scattering models; Galactic cosmic rays; Alpha particles

15. NUMBER OF PAGES
42

16. PRICE CODE
A03

17. SECURITY CLASSIFICATION OF REPORT	18. SECURITY CLASSIFICATION OF THIS PAGE	19. SECURITY CLASSIFICATION OF ABSTRACT	20. LIMITATION OF ABSTRACT
Unclassified	Unclassified		

NSN 7540-01-280-5500

Standard Form 298(Rev. 2-89)
Prescribed by ANSI Std. Z39-18
298-102

NASA-Langley, 1993